Eur. Phys. J. C (2025) 85:917
https://doi.org/10.1140/epjc/s10052-025-14636-6

THE EUROPEAN
PHYSICAL JOURNAL C

Regular Article - Theoretical Physics

Neutrino masses and mixing in an axion model

Sin Kyu Kang[1,a], **Hiroshi Okada**[2,b]

[1] School of Natural Science, Seoul National University of Science and Technology, Seoul 01811, Korea
[2] Department of Physics, Henan Normal University, Xinxiang 453007, China

Received: 7 May 2025 / Accepted: 9 August 2025

Abstract We propose a novel framework that simultaneously addresses three critical issues: tiny neutrino masses and their mixing patterns, dark matter, and the strong CP problem. Our model extends the Peccei–Quinn (PQ) symmetry by incorporating modular S_3 symmetry, which plays a central role in explaining the observed neutrino mixing structure. The field content includes two vector-like colored fermions and three colored scalars as S_3 singlets, an isospin doublet inert scalar and a singlet PQ scalar, each assigned appropriate modular weights. We show that such an extension, together with a suitable assignment of modular weights to the fields, can lead to holomorphic modular forms of Yukawa interactions, which can be derived from a superpotential. Furthermore, we explore an extension of the model to include non-holomorphic Yukawa interactions in the non-supersymmetric framework and show that the results are distinct from the holomorphic case. Tiny neutrino masses are generated radiatively through colored mediators, while the KSVZ-type axion appears to dynamically resolve the strong CP problem. We investigate the phenomenology of lepton flavor violation and the muon $g-2$ anomaly within this framework. Additionally, we explore the axion's properties and its role as dark matter.

1 Introduction

Despite the considerable success of the Standard Model (SM), it falls short in explaining the tiny neutrino masses [1,2] and cosmological dark matter (DM) [3,4]. To address these shortcomings, new physics beyond the SM is necessary. The most widely accepted mechanism for generating tiny neutrino masses is the seesaw mechanism, while the weakly interacting massive particle (WIMP) has long been considered as a strong candidate for DM. Another enduring issue in the SM is the strong charge-parity (CP) problem in Quantum Chromodynamics (QCD), which involves the unexpectedly small value of the CP-violating phase parameter $\bar{\theta}$. The Peccei–Quinn (PQ) mechanism [5,6] offers an elegant solution by introducing a new symmetry that, when spontaneously broken, results in a pseudo-Goldstone boson called the axion [7,8]. This mechanism effectively nullifies the CP-violating phase, providing a dynamic solution to the problem. Axion models, such as the KSVZ [9,10] and DFSZ [11,12] types, vary in whether SM quarks or exotic quarks carry the PQ charge.

While most extensions of the SM address these problems separately, there have been efforts to explore their connections. The scotogenic scenario simultaneously accommodates neutrino mass generation and a DM candidate, with neutrino masses arising radiatively from the exchange of DM states [13–15]. On the other hand, axions produced non-thermally in the early Universe via the so-called misalignment mechanism [16–18], can serve as excellent alternatives [19,20] to the WIMP DM [21]. There have also been investigations into embedding realize the DFSZ or KSVZ axion within the type-I seesaw model to address both issues coherently [22–25].

Recently, a novel idea has been proposed in which neutrino masses are generated at the quantum level through colored mediators that also resolve the strong CP problem. This new class of KSVZ-type axion models address key issues simultaneously: tiny neutrino masses, DM and the strong CP problem [26].

In this work, we extend the model to account for the observed neutrino mixing inferred from neutrino oscillation experiments by imposing S_3 modular symmetry on leptons and scalars [27–32], known as the minimal non-Abelian discrete flavor symmetry [33–37]. We introduce two vector-like fermions that transform as singlets under S_3, along with an isospin doublet inert scalar in the SM, both carrying nonzero modular weights. Neutrino masses are generated radiatively,

---

[a] e-mail: skkang@snut.ac.kr

[b] e-mail: hiroshi3okada@htu.edu.cn (corresponding author)

offering an attractive scenario that simultaneously explains the smallness of neutrino masses and provides a DM candidate. Additionally, we will examine several phenomenological aspects, including lepton flavor violations (LFVs), and the muon anomalous magnetic moment, and will discuss strategy for searching for axion DM.

Modular symmetry was originally introduced in the context of supersymmetry (SUSY) where the holomorphicity of modular forms arises naturally [28]. More recently, inspired by modular invariant theory based on automorphic forms [38], a non-supersymmetric formulation of the modular flavor symmetry has been proposed in Ref. [39]. In this work, we consider both SUSY and non-SUSY frameworks to explain lepton mixing and compare their resulting predictions. While both approaches yield nearly identical physical predictions for neutrino masses and mixing, the corresponding parameter space required to fit experimental data differ significantly. In SUSY framework, we suppress SUSY-related effects by assuming a high SUSY breaking scale and a small value of $\tan\beta$. Some remarks on this treatment will be provided below.

This paper is organized as follows. Section 2 introduces an axion framework designed to address tiny neutrino masses and mixing, dark matter and the strong CP problem. We incorporate modular S_3 symmetry to specifically explain neutrino mixing within the model. In Sect. 3, we demonstrate the leptonic Yukawa structures based on the proposed framework from Sect. 2. We also show how tiny neutrino masses are radiatively generated through a two-loop mechanism, followed by the results of a numerical analysis. Section 4 explores the phenomenology of lepton flavor violations and the anomaly of the lepton $g-2$. In Sect. 5, we discuss the properties of the axion and its role as dark matter within the framework. The conclusion and remarks are provided in Sect. 6. Additionally, reviews of two-loop integral of the neutrino masses and the modular S_3 symmetry are provided in the Appendices.

2 Framework

The model we consider is an extension of the original KSVZ model [9,10]. As in the KSVZ model, we introduce vector-like fermions Ψ_{L_i} and Ψ_{R_i} which are triplets under the fundamental representation of $\mathrm{SU}(3)_c$, singlets under $\mathrm{SU}(2)_L$, and with $Y=0$. To explain the observed neutrino mixing by imposing a flavor symmetry, we introduce two generations of the vector-like fermions. A complex scalar singlet σ is also introduced to break a $\mathrm{U}(1)_{\mathrm{PQ}}$ symmetry spontaneously, providing masses to those exotic fermions. The phase of σ corresponds to the axion field a. The differing PQ charges of Ψ_{L_i,R_i} ensure the anomalous axion-gluon coupling necessary to resolve the strong CP problem. Note that nonzero PQ charge ω is assigned to Ψ_{L_i}, while Ψ_{R_i} carries no PQ charge.

As proposed in [26], the vector-like fermion $\Psi_{L,R}$ fields can serve as mediators for neutrino mass generation at the two-loop level. To facilitate this process, two additional scalars, η and χ with the same $\mathrm{SU}(3)_c$ triplet representation, are introduced. These scalars contribute to the generation of neutrino masses at the two-loop level. While $\Psi_{L,R}$ and χ are hyperchargeless and transform as $\mathrm{SU}(2)_L$ singlets, $\eta \equiv [\eta^+, \eta^0]^T$ has $Y = 1/2$ and transforms as a $\mathrm{SU}(2)_L$ doublet. As mentioned, the $\mathrm{U}(1)_{\mathrm{PQ}}$ symmetry is spontaneously broken by non-zero vacuum of the complex scalar singlet σ with nonzero PQ charge ω, which also generates the masses of $\Psi_{L,R}$. Since the $\mathrm{SU}(3)_c$ invariant term arising from $\mathbf{3}\otimes\mathbf{3}\otimes\mathbf{3}$ is antisymmetric, we introduce three χ_i(with $i=1,2,3$) to allow trilinear term that is essential for generating neutrino masses at the two-loop level, and two copies of the colored fermion Ψ_i. And we note that terms involving $\overline{\Psi^c_{R_i}}\Psi_{R_i}$ and $\overline{\Psi^c_{L_i}}\Psi_{L_i}$ are not allowed. Table 1 lists all the new fields and their transformation properties under the SM and PQ symmetries.

To elucidate the neutrino mixing and masses observed in neutrino oscillation experiments, we enforce modular S_3 symmetry on the leptons and scalars. The leptons $\bar{L}_{L_2} \equiv (\overline{L_{L_\mu}}, \overline{L_{L_\tau}})^T$ and $e_{R_2} \equiv (e_{R_\mu}, e_{R_\tau})^T$ are organized into doublets ($\mathbf{2}$) under S_3, while the remaining leptons and scalars are singlets ($\mathbf{1}$) under S_3. Specifically, Ψ_{L_1} and Ψ_{R_1} transform as $\mathbf{1}$, while Ψ_{L_2} and Ψ_{R_2} transform as $\mathbf{1}'$ under S_3. The scalar fields (χ_1, χ_2, χ_3) are assigned to be $(\mathbf{1}', \mathbf{1}, \mathbf{1})$ under S_3. The modular weights k assigned to the fields are listed in Table 1, and those assigned to the modular forms of Yukawa couplings can be found in Table 2. We also impose Z_2 symmetry to prevent unwanted terms such as $(\eta^\dagger H)(\chi_2\chi_3)$ from being generated in the Lagrangian and scalar potential where H is the SM Higgs boson. Then, as will become evident later, neutrino masses are generated through solely the two-loop diagram shown in Fig. 1.

Imposing the modular S_3 symmetry, supplemented by PQ symmetry and an additional Z_2 symmetry together with the assignment of modular weight, we may construct holomorphic forms for Yukawa couplings and scalar potential terms, which can be derived from superpotential when we consider SUSY framework. This construction reflects that even non-SUSY framework is as robust as its SUSY counterpart by prohibiting undesirable terms and maintaining consistency at tree level. While holomorphicity of yukawa structure can be protected by SUSY, non-holomorphic terms can be arisen at loop level, which are suppressed compared to leading contributions arisen at tree level. Then, both approaches yield nearly identical results for neutrino masses and mixing.

Table 1 Field contents of fermions and bosons and their charge assignments under $SU(3)_c \otimes SU(2)_L \otimes U(1)_Y \otimes S_3 \otimes Z_2 \otimes U(1)_{\rm PQ}$ in the lepton and boson sector, where $-k$ is the number of modular weight and the quark sector is the same as the SM. $L_{L_2} \equiv (L_\mu, L_\tau)$, and $e_{R_2} \equiv (e_{R_\mu}, e_{R_\tau})$

	Fermions								Bosons					
	$\overline{L_{L_e}}$	$\overline{L_{L_2}}$	e_{R_e}	e_{R_2}	Ψ_{L_1}	Ψ_{L_2}	Ψ_{R_1}	Ψ_{R_2}	H	η^*	σ	χ_1	χ_2	χ_3
$SU(3)_c$	$\mathbf{1}$	$\mathbf{1}$	$\mathbf{1}$	$\mathbf{1}$	$\mathbf{3}$	$\mathbf{3}$	$\mathbf{3}$	$\mathbf{3}$	$\mathbf{1}$	$\mathbf{3}$	$\mathbf{1}$	$\mathbf{3}$	$\mathbf{3}$	$\mathbf{3}$
$SU(2)_L$	$\mathbf{2}$	$\mathbf{2}$	$\mathbf{1}$	$\mathbf{1}$	$\mathbf{1}$	$\mathbf{1}$	$\mathbf{1}$	$\mathbf{1}$	$\mathbf{2}$	$\mathbf{2}$	$\mathbf{1}$	$\mathbf{1}$	$\mathbf{1}$	$\mathbf{1}$
$U(1)_Y$	$\frac{1}{2}$	$\frac{1}{2}$	-1	-1	0	0	0	0	$\frac{1}{2}$	$-\frac{1}{2}$	0	0	0	0
$U(1)_{\rm PQ}$	0	0	0	0	w	w	0	0	0	0	w	0	0	0
S_3	$\mathbf{1}$	$\mathbf{2}$	$\mathbf{1}$	$\mathbf{2}$	$\mathbf{1}$	$\mathbf{1'}$	$\mathbf{1}$	$\mathbf{1'}$	$\mathbf{1}$	$\mathbf{1}$	$\mathbf{1}$	$\mathbf{1'}$	$\mathbf{1}$	$\mathbf{1}$
Z_2	1	1	1	1	-1	-1	-1	-1	1	-1	1	1	-1	-1
$-k$	-2	-2	-2	0	-2	-2	-2	-2	0	-2	0	-2	-2	-2

These bold-faced numbers mean group representations; 1 = singlet, 2 = doublet, 3 = triplet, and so on

Table 2 Modular weight assignments for Yukawa interaction

	Couplings						
	$Y_{\mathbf{1}}^{(4)}$	$Y_{\mathbf{1}}^{(6)}$	$Y_{\mathbf{1'}}^{(6)}$	$Y_{\mathbf{1}}^{(8)}$	$Y_{\mathbf{2}}^{(2)}$	$Y_{\mathbf{2}}^{(4)}$	$Y_{\mathbf{2}}^{(6)}$
S_3	$\mathbf{1}$	$\mathbf{1}$	$\mathbf{1'}$	$\mathbf{1}$	$\mathbf{2}$	$\mathbf{2}$	$\mathbf{2}$
$-k$	4	6	6	8	2	4	6

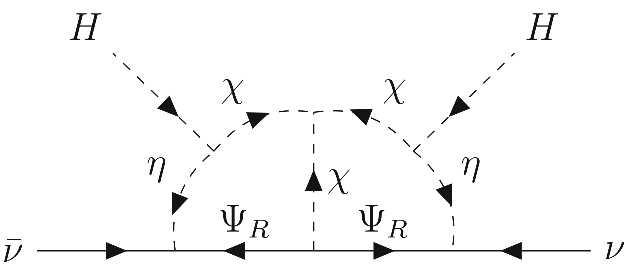

Fig. 1 Feynman diagram for two-loop neutrino mass

2.1 holomorphic case

Based on these symmetries, we can construct a renormalizable Yukawa Lagrangian for lepton sector as follows:

$$\begin{aligned}
-\mathcal{L}_{Lepton} &= \alpha_\ell (Y_{\mathbf{2}}^{(2)} \otimes \overline{L_{L_2}} \otimes e_{R_2})_{\mathbf{1}} H \\
&+ \beta_\ell (Y_{\mathbf{2}}^{(4)} \otimes \overline{L_{L_2}} \otimes e_{R_e})_{\mathbf{1}} H \\
&+ \gamma_\ell (Y_{\mathbf{2}}^{(2)} \otimes \overline{L_{L_e}} \otimes e_{R_2})_{\mathbf{1}} H + \delta_\ell (Y_{\mathbf{1}}^{(4)} \otimes \overline{L_{L_e}} \otimes e_{R_e})_{\mathbf{1}} H \\
&+ \alpha_\nu (Y_{\mathbf{2}}^{(6)} \otimes \overline{L_{L_2}} \otimes \Psi_{R_2})_{\mathbf{1}} \tilde{\eta} + \beta_\nu (Y_{\mathbf{1'}}^{(6)} \otimes \overline{L_{L_e}} \otimes \Psi_{R_2})_{\mathbf{1}} \tilde{\eta} \\
&+ \rho_\nu (Y_{\mathbf{1}}^{(6)} \otimes \overline{L_{L_e}} \otimes \Psi_{R_1})_{\mathbf{1}} \tilde{\eta} + \sigma_\nu (Y_{\mathbf{2}}^{(6)} \otimes \bar{L}_{L_2} \otimes \Psi_{R_1})_{\mathbf{1}} \tilde{\eta} \\
&+ \xi_0 (Y_{\mathbf{1}}^{(6)} \otimes \Psi_{R_1} \otimes \Psi_{R_2})_{\mathbf{1'}} \chi_1 \\
&+ \xi_1 (Y_{\mathbf{1}}^{(6)} \otimes \Psi_{R_2} \otimes \Psi_{R_1})_{\mathbf{1'}} \chi_1 \\
&+ \zeta_1 (\overline{\Psi_{L_1}} \otimes \Psi_{R_1})_{\mathbf{1}} \sigma + \zeta_2 (\overline{\Psi_{L_2}} \otimes \Psi_{R_2})_{\mathbf{1}} \sigma + \text{h.c.}, \qquad \text{(II.1)}
\end{aligned}$$

where $\tilde{\eta} \equiv i\sigma_2 \eta^*$, σ_2 being second Pauli matrix, $\zeta_{1(2)} = c_{1(2)}/(-i\tau + i\bar{\tau})^2$.[1] For simplicity, we omit color and SU$(2)_L$ indices. This leptonic Lagrangian can be derived from a superpotential, so it can be embedded in the SUSY framework.

2.2 Non-holomorphic case

The non-holomorphic modular flavor symmetry extends the original holomorphic modular invariance by incorporating polyharmonic Maaß forms [39,40]. While holomorphic modular forms are restricted to carry non-negative integer weights, non-holomorphic modular forms may possess negative integer weights, thereby broadening the scope of modular flavor model building. In this work, we extend the framework by introducing non-holomorphic modular form known as the polyharmonic Maaß form of $SL(2, Z)$. The minimal extension involves the inclusion of the polyharmonic Maaß form of $Y_{\mathbf{1}}^{(2)}$ which serves as a modular Yukawa coupling that transforms as a singlet under S_3 and carries modular weight 2. The explicit form of $Y_{\mathbf{1}}^{(2)}$ will be given in Sect. 3. The resulting non-holomorphic Yukawa term added to the Lagrangian Eq. (II.1) takes the following form,

$$\begin{aligned}
\sigma'_\ell Y_{\mathbf{1}}^{(2)} \otimes (\overline{L_{L_2}} \otimes e_{R_2})_{\mathbf{1}} H + \text{h.c.} &\equiv \sigma_\ell (L_{L_\mu} e_{R_\mu} \\
&+ L_{L_\tau} e_{R_\tau}) H + \text{h.c.}, \qquad \text{(II.2)}
\end{aligned}$$

---

[1] The invariance under the modular S_3 symmetry is discussed in Appendix C.

where σ_ℓ is an effective coupling constant arising from the modular form.

The scalar potential, invariant under $SU(3)_c \otimes SU(2)_L \otimes U(1)_Y \otimes S_3 \otimes Z_2 \otimes U(1)_{\rm PQ}$, is given by

$$\begin{aligned}\mathcal{V} = &-\mu_H^2|H|^2 + \mu_\eta^2|\eta|^2 + \mu_{\chi_i}^2|\chi_i|^2 + \mu_\sigma^2|\sigma|^2\\ &+ Y_{\mathbf{1}'}^{(6)}\mu_3\chi_1\chi_2\chi_3 + Y_{\mathbf{1}}^{(4)}\kappa_k\eta^\dagger H\chi_k + \text{h.c.}\\ &+ \frac{1}{4}\lambda_H|H|^4 + \frac{1}{4}\lambda_\sigma|\sigma|^4\\ &+ |Y_{\mathbf{1}}^{(8)}|\left(\frac{1}{4}\lambda_\eta|\eta|^4 + \frac{1}{4}\lambda_{\chi_i}|\chi_i|^4 + \lambda_{\eta\chi_i}|\eta|^2|\chi_i|^2\right)\\ &+ |Y_{\mathbf{1}}^{(4)}|\lambda_{\eta\sigma}|\eta|^2|\sigma|^2 + \lambda_{H\sigma}|H|^2|\sigma|^2\\ &+ |Y_{\mathbf{1}}^{(4)}|(\lambda_{\chi_i\sigma}|\chi_i|^2|\sigma|^2 + \lambda_{H\chi_i}|H|^2|\chi_i|^2)\\ &+ |Y_{\mathbf{1}}^{(4)}|(\lambda_{H\eta}|H|^2|\eta|^2 + \lambda'_{H\eta}|H^\dagger\eta|^2), \end{aligned} \tag{II.3}$$

where $i = 1, 2, 3$, $k = 2, 3$, $\mu_\eta^2 \equiv \tilde{\mu}_\eta^2/(-i\tau + i\bar{\tau})^2$, and $\mu_{\chi_i}^2 \equiv \tilde{\mu}_{\chi_i}^2/(-i\tau + i\bar{\tau})^2$. To preserve the SU(3)$_c$ symmetry the colored scalars η and $\chi_{1,2,3}$ must not acquire a vacuum expectation value (VEV), so that the only VEVs are $\langle\sigma\rangle = v_\sigma/\sqrt{2}$ breaking U(1)$_{\rm PQ}$, and $\langle H\rangle = [0, v_H/\sqrt{2}]^T$ ($v_H/\sqrt{2} \simeq 174$ GeV) triggering electroweak (EW) symmetry breaking. After EW symmetry breaking, mixing masses between η and χ_i are generated, which result in a mixing between η^0 and $\chi_i (= 2, 3)$. The squared-mass matrix is given by

$$M_{\eta\chi}^2 = \begin{bmatrix} \mu_\eta^2 & Y_{\mathbf{1}}^{(4)}\kappa_2 v' & Y_{\mathbf{1}}^{(4)}\kappa_3 v' \\ Y_{\mathbf{1}}^{(4)}\kappa_2 v' & \mu_{\chi_2}^2 & 0 \\ Y_{\mathbf{1}}^{(4)}\kappa_3 v' & 0 & \mu_{\chi_3}^2 \end{bmatrix}, \tag{II.4}$$

where $v' = v_H/\sqrt{2}$, and we have ignored the contributions from v_σ by assuming the coupling constants associated with σ are very small. Then, the scalar fields (η^0, χ_i) are expressed in terms of the mass eigenstates denoted by S_i as follows,

$$\begin{pmatrix} \eta^0 \\ \chi_2 \\ \chi_3 \end{pmatrix} = U \cdot \begin{pmatrix} S_1 \\ S_2 \\ S_3 \end{pmatrix}, \tag{II.5}$$

where U is a 3×3 unitary matrix that diagonalizes the matrix $M_{\eta\chi}^2$. The masses of S_i are denoted as m_{S_i} and the mass of χ_1 is denoted as m_{χ_1}.

It is worthwhile to notice that the Yukawa structures presented above may receive potential corrections. As discussed in [41], the primary sources of such corrections include higher dimensional operators, renormalization group (RG) evolution and SUSY breaking effects. The higher dimensional operators, though in principle allowed, are strongly constrained by the imposed symmetries and can be safely suppressed by assuming a large cutoff scale (i.e., the scale of new physics). As a result, their impacts on the predicted flavor structures can be negligible. RG corrections arising from the running of parameters from the high energy scale down to the electroweak scale can modify the predictions, but their effects become negligibly small in SUSY case if we assume a low $\tan\beta$ and a sufficiently high SUSY breaking scale. Even in non-SUSY case, RG effects can be kept under control by assuming a strongly hierarchical neutrino mass spectrum, masses of TeV scale mediators and no large Yukawa couplings in the lepton sectors. The SUSY breaking effects can also be ignorable under the same conditions of low $\tan\beta$ and high SUSY breaking scale, as discussed in [41]. Therefore, in this work, we will neglect these corrections and focus on the leading-order predictions based on the modular symmetry framework.

3 Leptonic Yukawa structures and radiative neutrino mass generation

Now, let us demonstrate how the lepton mixing matrix can be predicted by imposing a modular S_3 symmetry in the lepton sector. The modular forms with the lowest weight 2, $Y_{\mathbf{2}}^{(2)} \equiv (y_1, y_2)^T$, transforming as a doublet of S_3 is written in terms of Dedekind eta-function $\eta(\tau)$ and its derivative [42] as follows:

$$\begin{aligned} y_1(\tau) &= \frac{i}{4\pi}\left(\frac{\eta'(\tau/2)}{\eta(\tau/2)} + \frac{\eta'((\tau+1)/2)}{\eta((\tau+1)/2)} - \frac{8\eta'(2\tau)}{\eta(2\tau)}\right),\\ y_2(\tau) &= \frac{\sqrt{3}i}{4\pi}\left(\frac{\eta'(\tau/2)}{\eta(\tau/2)} - \frac{\eta'((\tau+1)/2)}{\eta((\tau+1)/2)}\right). \end{aligned} \tag{III.1}$$

Then, any couplings of higher weight are constructed by multiplication rules of S_3 as presented in Appendix B, and we find the following couplings [42]:

$$\begin{aligned} &Y_{\mathbf{1}}^{(4)} = y_1^2 + y_2^2, \quad Y_{\mathbf{1}}^{(6)} = 3y_1^2y_2 - y_2^3, \quad Y_{\mathbf{1}'}^{(6)} = y_1^3 - 3y_1y_2^2,\\ &Y_{\mathbf{2}}^{(4)} \equiv \begin{bmatrix} Y_{\mathbf{2},1}^{(4)} \\ Y_{\mathbf{2},2}^{(4)} \end{bmatrix} = \begin{bmatrix} 2y_1y_2 \\ y_1^2 - y_2^2 \end{bmatrix},\\ &Y_{\mathbf{2}}^{(6)} \equiv \begin{bmatrix} Y_{\mathbf{2},1}^{(6)} \\ Y_{\mathbf{2},2}^{(6)} \end{bmatrix} = \begin{bmatrix} y_1^3 + y_1y_2^2 \\ y_2^3 + y_1^2y_2 \end{bmatrix}. \end{aligned} \tag{III.2}$$

Note that the modular forms given above are holomorphic.

In contrast, the polyharmonic Maaß form $Y_{\mathbf{1}}^{(2)}$ is constructed from the modified Eisenstein series $\hat{E}_2(\tau)$ [40], which is a well-known example of a non-holomorphic modular form. It is explicitly defined as

$$Y_{\mathbf{1}}^{(2)}(\tau) = \hat{E}_2(\tau) = 1 - \frac{3}{\pi y} - 24\sum_{n=1}^{\infty}\sigma_1(n)q^n, \tag{III.3}$$

where $y = \text{Im}\tau$, $q = e^{2\pi i\tau}$ and $\sigma_1(n) = \sum_{d|n} d$ denotes the sum of the positive divisors of the integer n. The non-holomorpicity of $\hat{E}_2(\tau)$ arises explicitly from its dependence on y. Its corresponding q-expansion is given by

$$\hat{E}_2(\tau) = 1 - \frac{3}{\pi y} - 24q - 72q^2 - 96q^3 - 168q^4 \\ -144q^5 - \cdots. \tag{III.4}$$

The structure of Yukawa couplings is determined by the modular symmetry. After the EW spontaneous symmetry breaking, the charged lepton mass matrix is given by

$$\text{Holomorphic case}: m_\ell = \frac{v_H}{\sqrt{2}} \begin{bmatrix} \delta_\ell Y_1^{(4)} & \gamma_\ell y_1 & \gamma_\ell y_2 \\ \beta_\ell Y_{\mathbf{2},1}^{(4)} & \alpha_\ell y_2 & \alpha_\ell y_1 \\ \beta_\ell Y_{\mathbf{2},2}^{(4)} & \alpha_\ell y_1 & -\alpha_\ell y_2 \end{bmatrix}, \tag{III.5}$$

$$\text{Non-holomorphic case}: m_\ell \\ = \frac{v_H}{\sqrt{2}} \begin{bmatrix} \delta_\ell Y_1^{(4)} & \gamma_\ell y_1 & \gamma_\ell y_2 \\ \beta_\ell Y_{\mathbf{2},1}^{(4)} & \alpha_\ell y_2 + \sigma_\ell & \alpha_\ell y_1 \\ \beta_\ell Y_{\mathbf{2},2}^{(4)} & \alpha_\ell y_1 & -\alpha_\ell y_2 + \sigma_\ell \end{bmatrix}. \tag{III.6}$$

Then the charged lepton mass eigenstates and corresponding mass-squared eigenvalues can be obtained by diagonalizing the hermitian matrix $m_\ell m_\ell^\dagger$ as $V_{e_L}^\dagger m_\ell m_\ell^\dagger V_{e_L} = \text{diag.}(|m_e|^2, |m_\mu|^2, |m_\tau|^2)$, where V_{e_L} denotes the unitary matrix transforming left-handed charged leptons into the mass eigenstates.

The Dirac Yukawa matrix is given by

$$y_D = \begin{bmatrix} \rho_\nu Y_{\mathbf{1}}^{(6)} & \beta_\nu Y_{\mathbf{1'}}^{(6)} \\ \sigma_\nu Y_{\mathbf{2},1}^{(6)} & -\alpha_\nu Y_{\mathbf{2},2}^{(6)} \\ \sigma_\nu Y_{\mathbf{2},2}^{(6)} & \alpha_\nu Y_{\mathbf{2},1}^{(6)} \end{bmatrix}. \tag{III.7}$$

Since the scalar η can not have a nonzero VEV, the light neutrino masses can not be generated at tree level.

The mass matrix for the heavy colored fermions (Ψ_{L_1}, Ψ_{L_2}, Ψ_{R_1}, Ψ_{R_2}) is given by

$$M_\Psi = \frac{v_\sigma}{\sqrt{2}} \begin{bmatrix} 0 & 0 & \zeta_1 & 0 \\ 0 & 0 & 0 & \zeta_2 \\ \zeta_1 & 0 & 0 & 0 \\ 0 & \zeta_2 & 0 & 0 \end{bmatrix}. \tag{III.8}$$

The mass eigenvalues of $\Psi_{1,2}$ are found by $M_{1,2} \equiv \frac{v_\sigma}{\sqrt{2}} \zeta_{1,2}$.

The Yukawa and scalar interactions described in Eqs. (II.1) and (II.3) can generate Majorana neutrino masses at the two-loop level, as illustrated by the diagram in Fig. 1. A distinctive aspect of neutrino mass generation is that the masses of the neutrinos are mediated by the colored particles Ψ, η, and χ, all of which transform under the same $SU(3)_c$ representation. While η is a $SU(2)_L$ doublet, Ψ and χ are $SU(2)_L$ singlets. The coupling between L and Ψ necessitates that η has a hypercharge $Y = 1/2$. In our scenario Ψ and χ carry no hypercharge, which ensures the Majorana nature of light neutrinos.

The Lagrangian terms contributing to neutrino masses arisen at two loop are written as

$$\mathcal{L} \supset [\alpha_\nu (Y_{\mathbf{2},1}^{(6)} \bar{\nu}_\tau - Y_{\mathbf{2},2}^{(6)} \bar{\nu}_\mu) + \beta_\nu Y_{\mathbf{1'}}^{(6)} \bar{\nu}_e] \Psi_{R_2} \tilde{\eta} \\ + [\rho_\nu Y_{\mathbf{1}}^{(6)} \bar{\nu}_e + \sigma_\nu (Y_{\mathbf{2},1}^{(6)} \bar{\nu}_\mu + Y_{\mathbf{2},2}^{(6)} \bar{\nu}_\tau)] \Psi_{R_1} \tilde{\eta} \\ + [\xi_0 Y_{\mathbf{1}}^{(6)} \overline{\Psi_{R_1}^C} \Psi_{R_2} + \xi_1 Y_{\mathbf{1}}^{(6)} \overline{\Psi_{R_2}^C} \Psi_{R_1}] \chi_1 \\ + Y_{\mathbf{1}}^{(6)} \mu_3 \chi_1 \chi_2 \chi_3 + Y_{\mathbf{1}}^{(4)} (\kappa_2 \chi_2 + \kappa_3 \chi_3) \eta^\dagger H. \tag{III.9}$$

Then, the combinations of the couplings for neutrino mass generation are denoted as follows;

$$\mathcal{Y}^1 = \mathcal{C}^1 \cdot \begin{pmatrix} (\beta_\nu Y_{\mathbf{1'}}^{(6)} \cdot \rho_\nu^* Y_{\mathbf{1}}^{(6)*}) & (\beta_\nu Y_{\mathbf{1'}}^{(6)} \cdot \sigma_\nu^* Y_{\mathbf{2},1}^{(6)*}) & (\beta_\nu Y_{\mathbf{1'}}^{(6)} \cdot \sigma_\nu^* Y_{\mathbf{2},2}^{(6)*}) \\ (\beta_\nu Y_{\mathbf{1'}}^{(6)} \cdot \sigma_\nu^* Y_{\mathbf{2},1}^{(6)*}) & -(\alpha_\nu Y_{\mathbf{2},2}^{(6)} \cdot \sigma_\nu^* Y_{\mathbf{2},1}^{(6)*}) & -(\alpha_\nu Y_{\mathbf{2},2}^{(6)} \cdot \sigma_\nu^* Y_{\mathbf{2},2}^{(6)*}) \\ (\beta_\nu Y_{\mathbf{1'}}^{(6)} \cdot \sigma_\nu^* Y_{\mathbf{2},2}^{(6)*}) & -(\alpha_\nu Y_{\mathbf{2},2}^{(6)} \cdot \sigma_\nu^* Y_{\mathbf{2},2}^{(6)*}) & (\alpha_\nu Y_{\mathbf{2},1}^{(6)} \cdot \sigma_\nu^* Y_{\mathbf{2},2}^{(6)*}) \end{pmatrix}, \tag{III.10}$$

$$\mathcal{Y}^2 = \mathcal{C}^2 \cdot \begin{pmatrix} (\rho_\nu Y_{\mathbf{1}}^{(6)} \cdot \beta_\nu^* Y_{\mathbf{1'}}^{(6)*}) & -(\rho_\nu Y_{\mathbf{1}}^{(6)} \cdot \alpha_\nu^* Y_{\mathbf{2},2}^{(6)*}) & (\rho_\nu Y_{\mathbf{1}}^{(6)} \cdot \alpha_\nu^* Y_{\mathbf{2},1}^{(6)*}) \\ -(\rho_\nu Y_{\mathbf{1}}^{(6)} \cdot \alpha_\nu^* Y_{\mathbf{2},2}^{(6)*}) & -(\sigma_\nu Y_{\mathbf{2},1}^{(6)} \cdot \alpha_\nu^* Y_{\mathbf{2},2}^{(6)*}) & (\sigma_\nu Y_{\mathbf{2},1}^{(6)} \cdot \alpha_\nu^* Y_{\mathbf{2},1}^{(6)*}) \\ (\rho_\nu Y_{\mathbf{1}}^{(6)} \cdot \alpha_\nu^* Y_{\mathbf{2},1}^{(6)*}) & (\sigma_\nu Y_{\mathbf{2},1}^{(6)} \cdot \alpha_\nu^* Y_{\mathbf{2},1}^{(6)*}) & (\sigma_\nu Y_{\mathbf{2},2}^{(6)} \cdot \alpha_\nu^* Y_{\mathbf{2},1}^{(6)*}) \end{pmatrix},$$

where $\mathcal{C}^1 \equiv \mu_3 \kappa_2 \kappa_3 \xi_1 (Y_{\mathbf{1}}^{(6)} \cdot Y_{\mathbf{1}}^{(4)})^2$ and $\mathcal{C}^2 \equiv \mu_3 \kappa_2 \kappa_3 \xi_0 (Y_{\mathbf{1}}^{(6)} \cdot Y_{\mathbf{1}}^{(4)})^2$. The light neutrino masses derived from the two-loop diagram are given by

$$(m_\nu)_{\alpha\beta} = \frac{N_c}{4(4\pi)^2} [\mathcal{Y}^1 L_{12} + \mathcal{Y}^2 L_{21}], \tag{III.11}$$

where $N_c (= 3)$ is the color factor. The loop functions L_{lm} are [43] [2]

$$L_{lm} = \int_0^1 dx dy dz \frac{\delta(x+y+z-1)}{(1-y)} \\ \times \left[\sum_{i=1}^{3} U_{1i}^2 U_{2i} U_{3i} \mathcal{I} \left(\frac{m_{S_i}^2}{M_m^2}, \frac{m_{S_i \Psi_l}^2}{M_m^2} \right) \right. \\ \left. - \sum_{i,j=1 (i \neq j)}^{3} U_{1i} U_{2i} U_{1j} U_{3j} \mathcal{I} \left(\frac{m_{S_i}^2}{M_m^2}, \frac{m_{S_j \Psi_l}^2}{M_m^2} \right) \right], \tag{III.12}$$

with

$$\mathcal{I}(a, b) = \frac{a^2 \ln a}{(1-a)(a-b)} - \frac{b^2 \ln b}{(1-b)(b-a)}, \\ \text{and} \quad m_{S_i \Psi_j}^2 = \frac{x m_{S_i}^2 + y M_j^2 + z m_{\chi_1}^2}{y(1-y)}. \tag{III.13}$$

The neutrino mass matrix m_ν is diagonalized by a unitary matrix U_ν as $U_\nu^\dagger m_\nu U_\nu^* = \text{diag}[D_{\nu_1}, D_{\nu_2}, D_{\nu_3}]$. Note here that, with only two copies of $\Psi (n_\Psi = 2)$, one of the three light neutrinos is predicted to be massless. Therefore, there is one Majorana phase and we define $\text{diag}[1, e^{\alpha_{21}/2}, 1]$ with $\alpha_{21} \neq 0$. Because of vanishing the lightest neutrino mass, the

---

[2] A brief derivation of the two-loop integral is presented in Appendix A.

other two neutrino mass eigenvalues are given in terms of two neutrino mass squared differences that are experimentally observed.

$$({\rm NH}):\ D_{\nu_2}\approx\sqrt{\Delta m^2_{\rm sol}},\quad D_{\nu_3}\approx\sqrt{|\Delta m^2_{\rm atm}|},\tag{III.14}$$

$$({\rm IH}):\ D_{\nu_1}\approx\sqrt{|\Delta m^2_{\rm atm}-\Delta m^2_{\rm sol}|},\quad D_{\nu_2}\approx\sqrt{|\Delta m^2_{\rm atm}|},\tag{III.15}$$

where NH and IH are respectively normal hierarchy and inverted hierarchy of neutrino masses. Since $\Delta m^2_{\rm sol}/\Delta m^2_{\rm atm} 1$ from the experiments, the sum of neutrino masses $\sum D_\nu$ is approximately given by

$$({\rm NH}):\ \sum D_\nu\approx\sqrt{|\Delta m^2_{\rm atm}|}\simeq 50\ {\rm meV},\tag{III.16}$$

$$({\rm IH}):\ \sum D_\nu\approx 2\sqrt{|\Delta m^2_{\rm atm}|}\simeq 100\ {\rm meV}.\tag{III.17}$$

Thus, the upper bound from the minimal cosmological model ΛCDM $+\sum D_\nu$; $\sum D_\nu\leq 120$ meV [4,44], is already satisfied. But recent combined data of DESI and CMB gives more stringent upper bound; $\sum D_\nu\leq 72$ meV [45]. If this experimental result is confirmed, IH would be disfavored. Then, the PMNS mixing matrix is given by $U_{\rm PMNS}=V^\dagger_{eL}U_\nu$. From the standard parameterization of $U_{\rm PMNS}$, the mixing angles are presented in terms of the entries of $U_{\rm PMNS}$ as follows:

$$s^2_{12}=\frac{|(U_{\rm PMNS})_{12}|^2}{1-|(U_{\rm PMNS})_{13}|^2},\quad s^2_{13}=|(U_{\rm PMNS})_{13}|^2,$$
$$s^2_{23}=\frac{|(U_{\rm PMNS})_{23}|^2}{1-|(U_{\rm PMNS})_{13}|^2},\tag{III.18}$$

where we have used short-hand notations $s^2_{12}(c^2_{12})$, $s^2_{13}(c^2_{13})$, $s^2_{23}(c^2_{23})$ for $\sin^2\theta_{12}(\cos^2\theta_{12})$, $\sin^2\theta_{13}(\cos^2\theta_{13})$, $\sin^2\theta_{23}$ $(\cos^2\theta_{23})$, respectively. As a constraint, we take into account the neutrinoless double beta decay whose amplitude is proportional to the effective neutrino mass given by

$$({\rm NH}):\langle m_{ee}\rangle$$
$$=|D_{\nu_2}s^2_{12}c^2_{13}e^{i\alpha_{21}}+D_{\nu_3}s^2_{13}e^{-2i\delta_{\rm CP}}|,\tag{III.19}$$

$$({\rm IH}):\langle m_{ee}\rangle=|D_{\nu_1}c^2_{12}c^2_{13}+D_{\nu_2}s^2_{12}c^2_{13}e^{i\alpha_{21}}|.\tag{III.20}$$

The most stringent bound on $\langle m_{ee}\rangle$ comes from KamLAND-Zen experiments whose upper bound is found as $\langle m_{ee}\rangle<$ (36–156) meV at 90% confidence level [46,47]. To constrain the model parameters, we will use the bound on $\langle m_{ee}\rangle$ from KamLAND-Zen experiment when our $\langle m_{ee}\rangle$ is nearby this bound.

3.1 Numerical results

For our numerical analysis, at first, we naively consider the experimentally allowed regions for the mass-squared differences and mixing parameters within the 3σ ranges in Nufit 5.0 [48] as follows:

$$({\rm NH}):|\Delta m^2_{\rm atm}|=[2.431-2.598]\times 10^{-3}\ {\rm eV}^2,$$
$$\Delta m^2_{\rm sol}=[6.82-8.04]\times 10^{-5}\ {\rm eV}^2,$$
$$s^2_{12}=[0.269-0.343],$$
$$s^2_{23}=[0.407-0.618],\quad s^2_{13}=[0.02034-0.02430].\tag{III.21}$$

$$({\rm IH}):|\Delta m^2_{\rm atm}|=[2.412-2.583]\times 10^{-3}\ {\rm eV}^2,$$
$$\Delta m^2_{\rm sol}=[6.82-8.04]\times 10^{-5}\ {\rm eV}^2,$$
$$s^2_{12}=[0.269-0.343],$$
$$s^2_{23}=[0.411-0.621],\quad s^2_{13}=[0.02053-0.02436].\tag{III.22}$$

However since the χ^2 of s_{23} is far from Gaussian form, we perform our χ^2 analysis more precisely, making the use of the reliable five data of Nufit5.0; $[\Delta m^2_{\rm atm},\Delta m^2_{\rm sol},s^2_{12},s^2_{23},s^2_{13}]$. Note that Dirac CP phase is considered as our output parameter, since wide region is allowed at 3σ. Based on the formulae for neutrino masses, mixing, charged lepton masses, and effective neutrino mass, we perform a parameter scan of the model. We randomly select data points that satisfy the experimental results for neutrino oscillation parameters within 5σ range and to bounds on experiments such as neutrinoless double beta decay. As explained earlier, this model predicts that the lightest neutrino is massless. Therefore, we set $D_{\nu_1(\nu_3)}=0$, considering the NH(IH) for neutrino mass spectrum, and retain only the nonzero Majorana phase α_{21}.

3.1.1 Holomorphic case

For the complex dimensionless parameters β_ν/ρ_ν, σ_ν/ρ_ν and a real parameter α_ν/ρ_ν, we scan over the absolute range $[10^{-5}-10^5]$. Since ρ_ν is an overall factor in the neutrino mass matrix, its specific value does not need to be fixed. As mentioned earlier, the free parameter for the charged lepton mass matrix is δ_l, which we scan over the range $[0.01-100]$. We note that the values of δ_l beyond 100 violate perturbativity but the total values are within the perturbative limit due to multiplication of modular coupling $Y^{(4)}_{\bf 1}$ as can be seen in Eq. (II.1). We also scan the relevant mass parameters $m_{\eta^\pm}$, $M_{1,2}$ in the range $[10^3-10^5]$ GeV. Note here that m_{S_i} $(i=1,2,3)$ are not needed to be fixed since there masses can be involved in overall factors of the neutrino mass matrix. Through a χ^2 analysis, we find that the best-fit values of the parameters are obtained at $\chi_{\rm min}=3.84$. The corresponding best-fit parameter values are listed in Table 3. IH of the holomorphic case is disfavored by the neutrino oscillation data, and we concentrate on the case of NH.

Table 3 Best-fit (BF) parameter values in the NH case corresponding to $\chi_{\rm min} = 3.84$

Parameter	BF	Parameter	BF	Parameter	BF
τ	$-0.072 + 1.918i$	$m_{\eta^\pm}$	1200.73 GeV	M_1	1171.5 GeV
M_2	23870 GeV	σ_ν/ρ_ν	$-0.0034 - 0.0362i$	α_ν/ρ_ν	-1.705
β_ν/ρ_ν	$-0.027 - 1.959i$	δ_l	$-3.742 + 20.796i$	α_l	0.0023
β_l	60.298	γ_l	0.504		
s_{12}	0.5317	s_{23}	0.7519	s_{13}	0.1504
$\Delta m^2_{\rm sol}$	7.353×10^{-5} eV^2	$\Delta m^2_{\rm atm}$	2.52×10^{-3} eV^2	$\delta_{\rm CP}$	345.951°
α_{21}	187.503°	$\sum D_\nu$	5.88×10^{-2} eV	$\langle m_{ee}\rangle$	1.37×10^{-3} eV

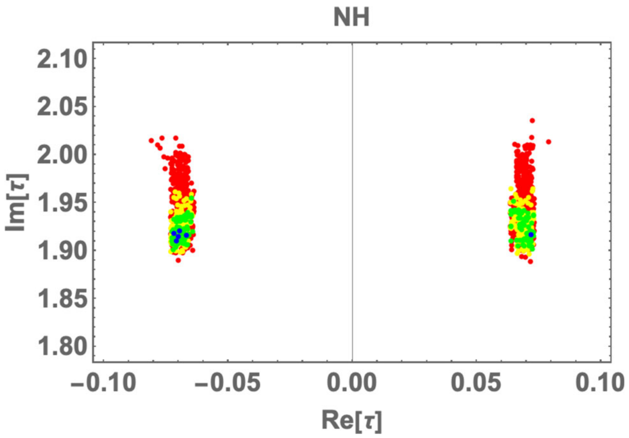

Fig. 2 Scatter plot for Re[τ] *vs.* Im[τ]. The red, yellow, green and blue points correspond to $3\sigma - 5\sigma$, $2\sigma - 3\sigma$, $1\sigma - 2\sigma$, and $0\sigma - 1\sigma$, respectively

Figure 2 shows scatter plot of the real and imaginary parts of the modulus τ constrained within 5σ. The red, yellow, green and blue points correspond to $3\sigma - 5\sigma$, $2\sigma - 3\sigma$, $1\sigma - 2\sigma$, and $0\sigma - 1\sigma$, respectively. From the plot, we see that the allowed regions of the modulus τ within the 5σ range confined to a relatively narrow space as $0.062 \lesssim |\text{Re}[\tau]| \lesssim 0.082$ and $1.88 \lesssim \text{Im}[\tau] \lesssim 2.04$.

Figure 3 represents scatter plots of (a) s^2_{23} (b) $\delta_{\rm CP}$ (c) α_{21} (d) $\langle m_{ee}\rangle$ in terms of $\sum D_\nu$. The color scheme for the data points is consistent with that in Fig. 2. The pink vertical dashed lines indicate the upper limit on the sum of neutrino masses from combined data of DESI and CMB. From the plots, the allowed range for $\sum D_\nu$ up to 5σ is between 57.2 meV and 60 meV. In panel (a), it is evident that larger values of s^2_{23} are favored. For the Dirac CP phase $\delta_{\rm CP}$, the allowed regions are approximately $0 \sim 20°$ and $335° \sim 350°$. In contrast, for the Majorana CP phase α_{21}, the allowed regions are approximately $157° \sim 166°$, $168° \sim 176°$, $183° \sim 191°$, and $195° \sim 202°$. The effective mass $\langle m_{ee}\rangle$ has an allowed region of 0.8meV $\sim$ 1.5meV, which is significantly below the current experimental bound from the current KamLAND-Zen experiment [46,47]. Figure 4 shows the correlation between α_{21} and $\delta_{\rm CP}$. Six distinct allowed regions can be identified in the plot.

3.1.2 *Non-holomorphic case*

In the non-holomorphic case, the charged lepton mass matrix includes an additional free parameter, σ_ℓ, as introduced in Eq. (II.2). We scan σ_ℓ over the absolute range $[10^{-5} - 10^5]$, keeping all other parameters and their respective scan ranges identical to those in the holomorphic case.

From a χ^2 analysis for the NH case, we find that the best-fit values of the parameters are obtained at $\chi_{\rm min} = 3.042$. The corresponding best-fit parameter values are listed in Table 4.

Figure 5 shows the scatter plot of the real and imaginary parts of the modulus τ constrained within 5σ region. The color legends are the same as the holomorphic case. From the plot, we see that the allowed region for the modulus τ is confined to a relatively narrow range, $0.025 \lesssim |\text{Re}[\tau]| \lesssim 0.145$ and $1.83 \lesssim \text{Im}[\tau] \lesssim 2.04$.

Figure 6 represents the scatter plots of (a) s^2_{23} (b) $\delta_{\rm CP}$ (c) α_{21} (d) $\langle m_{ee}\rangle$ in terms of $\sum D_\nu$. The color scheme for the data points is consistent with that in Fig. 2. The vertical pink dashed lines indicate the upper limit on the sum of neutrino masses derived from the combined data of DESI and CMB. From the plots, we find that the allowed range for $\sum D_\nu$ up to 5σ lies between 57.2 meV and 60 meV. Panel (a) represents a preference for larger values of s^2_{23}. For the Dirac CP phase $\delta_{\rm CP}$, the allowed regions are approximately $0 \sim 20°$ and $330° \sim 360°$. In contrast, for the Majorana CP phase α_{21}, the allowed region lies approximately in the region of $150° \sim 210°$. The effective mass $\langle m_{ee}\rangle$ is constrained to the range 0.9meV $\sim$ 1.83meV, which is significantly below the current experimental bound from the current KamLAND-Zen experiment [46,47]. Figure 7 shows the correlation between α_{21} and $\delta_{\rm CP}$. Six allowed regions could be identified in the plot.

From a χ^2 analysis for the IH case, we find that the best-fit values of the parameters are obtained at $\chi_{\rm min} = 7.82429$. The corresponding best-fit parameter values are listed in Table 5.

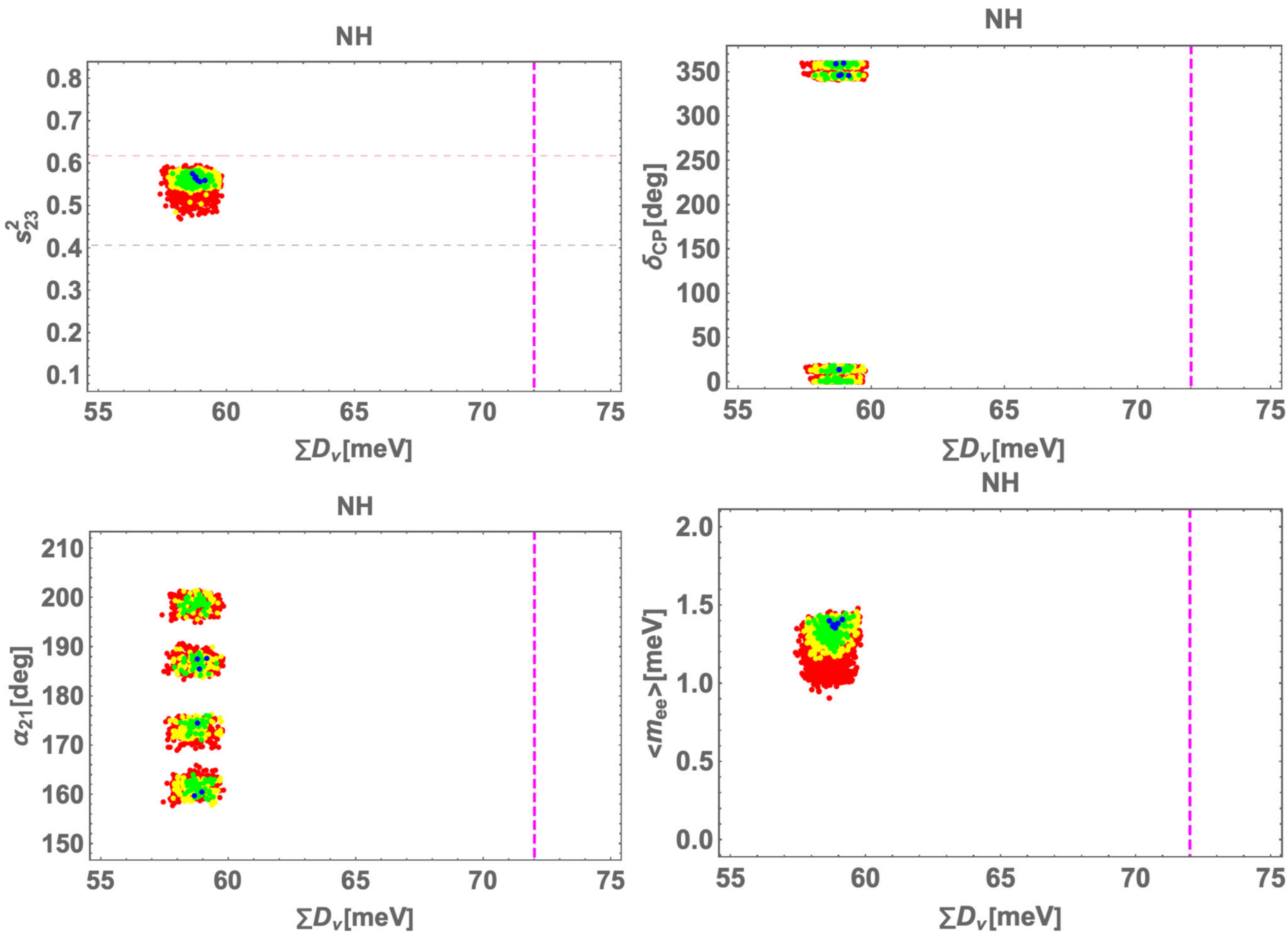

Fig. 3 Plots for **a** s^2_{23}, **b** δ_{CP}, **c** α_{21}, **d** $\langle m_{ee}\rangle$ *vs.* $\sum D_\nu$. The colors of the points carry the same meanings as in Fig. 2

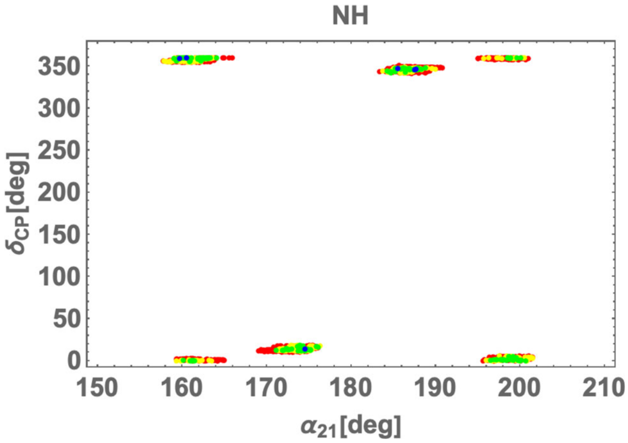

Fig. 4 Plot for the allowed regions of the parameter space $(\alpha_{21}, \delta_{\mathrm{CP}})$. The colors of the points carry the same meanings as in Fig. 2

Figure 8 shows the scatter plot for the real and imaginary parts of the modulus τ constrained. The color legends are the same as the holomorphic case. From the plot, we see that the allowed region of the modulus τ is confined to a relatively narrow region, $0.3 \lesssim |\mathrm{Re}[\tau]| \lesssim 0.4$ and $3.25 \lesssim \mathrm{Im}[\tau] \lesssim 3.50$.

Figure 9 represents the scatter plots of (a) s^2_{23} (b) δ_{CP} (c) α_{21} (d) $\langle m_{ee}\rangle$ in terms of $\sum D_\nu$. The color scheme for the data points is consistent with that in Fig. 2. The vertical pink(red) dashed lines indicate the upper limit on the sum of neutrino masses from combined data of DESI and CMB (cosmological observations). From the plots, the allowed range for $\sum D_\nu$ lies between 93 meV and 102 meV. Panel (a) shows a tendency toward smaller values of s^2_{23}. For the Dirac CP phase δ_{CP}, the allowed region is approximately $130^\circ \sim 220^\circ$. In contrast, for the Majorana CP phase α_{21}, the allowed region spans the full phase range. The effective mass $\langle m_{ee}\rangle$ lies between 10 meV and 17 meV, which is still below the current experimental bound from the current KamLAND-Zen experiment [46,47] whose line is indicated by the gray dotted one. Figure 10 shows the correlation between α_{21} and δ_{CP}. Unlike the NH case, no clear correlation is observed.

Table 4 Best-fit (BF) parameter values in the NH case corresponding to $\chi_{\min} = 3.042$

Parameter	BF	Parameter	BF	Parameter	BF
τ	$-0.088 + 1.861i$	$m_{\eta^\pm}$	1127.68 GeV	M_1	1439.18 GeV
M_2	26885.8 GeV	σ_ν/ρ_ν	$-0.0028 + 0.0426i$	α_ν/ρ_ν	-2.060
β_ν/ρ_ν	$-0.03219 + 2.375i$	δ_l	$-3.178 - 19.53i$	α_l	0.0021
β_l	60.707	γ_l	0.500	$\sigma_\ell \times 10^4$	$-2.338 - 2.566i$
s_{12}	0.5390	s_{23}	0.7645	s_{13}	0.1488
$\Delta m^2_{\mathrm{sol}}$	7.229×10^{-5} eV^2	$\Delta m^2_{\mathrm{atm}}$	2.530×10^{-3} eV^2	δ_{CP}	17.875°
α_{21}	179.363°	$\sum D_\nu$	0.0588 eV	$\langle m_{ee}\rangle$	1.63×10^{-3} eV

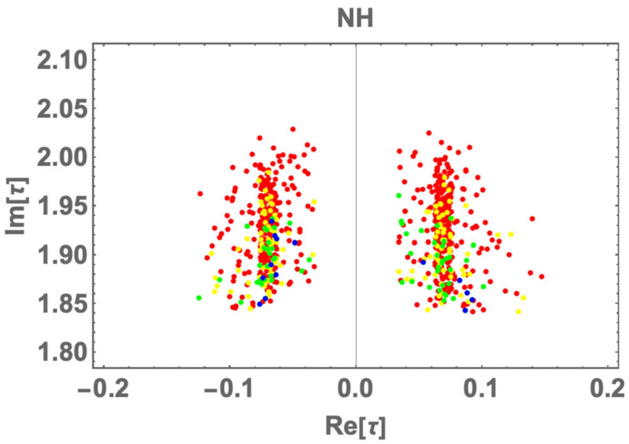

Fig. 5 Scatter plot for Re[τ] *vs.* Im[τ]. The red, yellow, green and blue points correspond to $3\sigma - 5\sigma$, $2\sigma - 3\sigma$, $1\sigma - 2\sigma$, and $0\sigma - 1\sigma$, respectively

4 Lepton flavor violation and lepton $g-2$

Lepton flavor violating (LFV) processes are induced by the Yukawa interactions $\overline{L_{L_i}}\tilde{\eta}\Psi_{R_j}$, and the relevant Lagrangian is given by

$$\mathcal{L} \supset (\beta_\nu Y^{(6)}_{\mathbf{1}'}\bar{e} - \alpha_\nu Y^{(6)}_{\mathbf{2},2}\bar{\mu} + \alpha_\nu Y^{(6)}_{\mathbf{2},1}\bar{\tau})\tilde{\eta}\Psi_{R_2} + (\rho_\nu Y^{(6)}_{\mathbf{1}}\bar{e} + \sigma_\nu Y^{(6)}_{\mathbf{2},1}\bar{\mu} + \sigma_\nu Y^{(6)}_{\mathbf{2},2}\bar{\tau})\tilde{\eta}\Psi_{R_1}. \tag{IV.1}$$

The matrix of Yukawa couplings for the interactions described above is given by Eq. (III.7). We consider the LFV processes $\ell_i \to \ell_j\gamma$ ($(l_1, l_2, l_3) \equiv (e, \mu, \tau)$), with $\mu \to e\gamma$ providing the most stringent constraint on the model parameter. The branching ratio of the LFV processes $\ell_i \to \ell_j\gamma$ is given by [49,50]

$$\mathrm{BR}(\ell_i \to \ell_j\gamma) \approx \frac{48\pi^3\alpha_e C_{ij}}{G_F^2(4\pi)^4}\left|\sum_{\alpha=1}^{2} y_{D_{j\alpha}} y^\dagger_{D_{\alpha i}} F(M_\alpha, m_{\eta^\pm})\right|^2, \tag{IV.2}$$

$$F(m_a, m_b) \approx \frac{2m_a^6 + 3m_a^4m_b^2 - 6m_a^2m_b^4 + m_b^6 + 12m_a^4m_b^2\ln\left(\frac{m_b}{m_a}\right)}{12(m_a^2 - m_b^2)^4}, \tag{IV.3}$$

where $C_{21} = 1$, $C_{31} = 0.1784$, $C_{32} = 0.1736$, $\alpha_e \approx 1/137$ is the fine structure constant, and $G_F = 1.166 \times 10^{-5}$ GeV^{-2}. The current experimental upper bounds are given by [51–53]

$$\begin{aligned} &\mathrm{BR}(\mu \to e\gamma) \lesssim 4.2 \times 10^{-13}, \\ &\mathrm{BR}(\tau \to e\gamma) \lesssim 3.3 \times 10^{-8}, \\ &\mathrm{BR}(\tau \to \mu\gamma) \lesssim 4.4 \times 10^{-8}. \end{aligned} \tag{IV.4}$$

Our numerical analysis reveals that the best fit values predict the branching ratios for $\mathrm{Br}(l_i \to l_j\gamma)$ as follows:

$$\begin{aligned} &\text{Holomorphic case(NH only)}: \\ &\mathrm{BR}(\mu \to e\gamma) \lesssim 5.97 \times 10^{-25}, \\ &\mathrm{BR}(\tau \to e\gamma) \lesssim 1.55 \times 10^{-23}, \\ &\mathrm{BR}(\tau \to \mu\gamma) \lesssim 1.19 \times 10^{-26}, \end{aligned} \tag{IV.5}$$

$$\begin{aligned} &\text{Non}-\text{holomorphic case}: \\ &\text{NH}:\ \mathrm{BR}(\mu \to e\gamma) \lesssim 9.60 \times 10^{-25}, \\ &\mathrm{BR}(\tau \to e\gamma) \lesssim 2.10 \times 10^{-23}, \\ &\mathrm{BR}(\tau \to \mu\gamma) \lesssim 2.27 \times 10^{-26}, \end{aligned} \tag{IV.6}$$

$$\begin{aligned} &\text{IH}:\ \mathrm{BR}(\mu \to e\gamma) \lesssim 2.63 \times 10^{-31}, \\ &\mathrm{BR}(\tau \to e\gamma) \lesssim 2.77 \times 10^{-25}, \\ &\mathrm{BR}(\tau \to \mu\gamma) \lesssim 3.14 \times 10^{-32}, \end{aligned} \tag{IV.7}$$

which are significantly below the current experimental bounds stated in Eq. (IV.4).

In a similar way as in the above LFVs, we can also formulate the muon and electron $g-2$ as follows:

$$\Delta a_l \approx -\frac{m_l^2}{(4\pi)^2}\sum_{\alpha=1}^{2}\left(y_{D_{l\alpha}} y^\dagger_{D_{\alpha l}}\right) F(M_\alpha, m_{\eta^\pm}), \tag{IV.8}$$

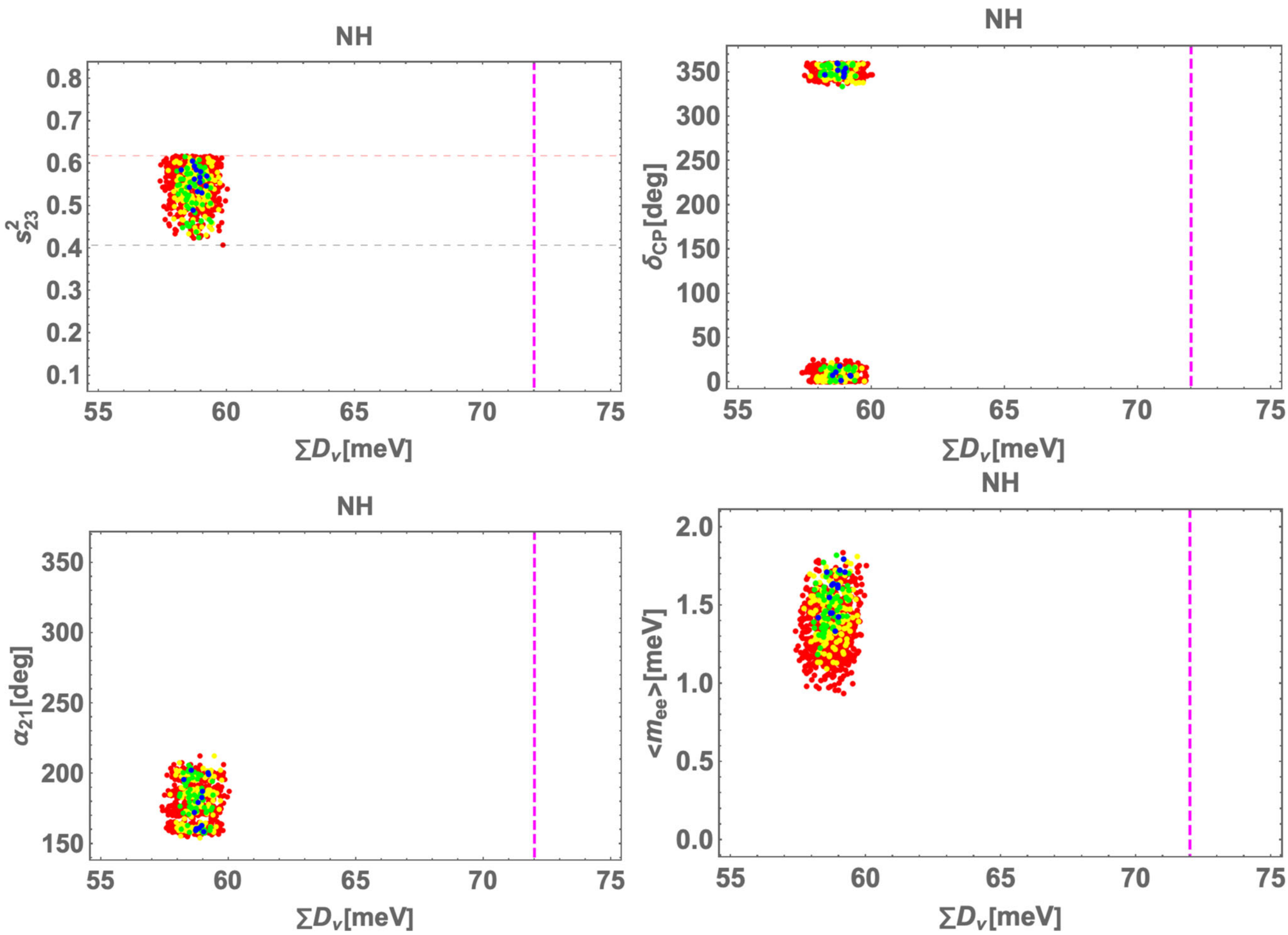

Fig. 6 Plots for **a** s^2_{23}, **b** $\delta_{\rm CP}$, **c** α_{21}, **d** $\langle m_{ee}\rangle$ *vs.* $\sum D_\nu$. The colors of the points carry the same meanings as in Fig. 2

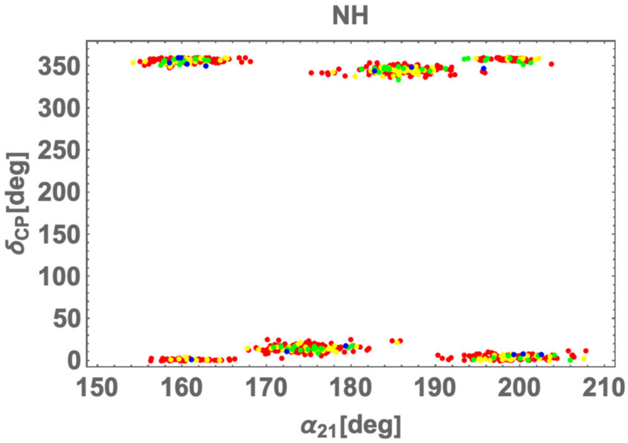

Fig. 7 Plot for the allowed regions of the parameter space $(\alpha_{21}, \delta_{\rm CP})$. The colors of the points carry the same meanings as in Fig. 2

where $l = e, \mu$. If $m_{\eta^\pm} = M_{1,2} = 100$ GeV, Eq. (IV.8) is simplified as follows:

$$|\Delta a_e| = 6.86 \times 10^{-15} \times \left(\sum_{\alpha=1}^{2} y_{D_{e\alpha}} y^\dagger_{D_{\alpha e}}\right) \lesssim 8.8 \times 10^{-13},$$

$$|\Delta a_\mu| = 2.95 \times 10^{-10} \times \left(\sum_{\alpha=1}^{2} y_{D_{\mu\alpha}} y^\dagger_{D_{\alpha\mu}}\right) \lesssim 2.61 \times 10^{-9}, \tag{IV.9}$$

where the constraints are set so that the new contributions do not exceed the current discrepancy between the experimental values and the SM predictions. These constraints can be expressed in terms of the Yukawa upper bounds as $y_D \simeq 4.61(1.21)$ for electron (muon) $g-2$, which are weaker than the constraint from $\mu \to e\gamma$.

5 Implications for invisible axion and dark matter

5.1 Invisible Axion

Decomposing the complex scalar field in polar coordinate, $\sigma = (v_\sigma + \rho)\exp(ia/v_\sigma)/\sqrt{2}$, the field a corresponds to the axion, while the radial mode has a mass term as well as cubic and quartic self-interactions in the scalar potential. In the PQ broken phase, we see the fermion Ψ_i gets massive

Table 5 Best-fit (BF) parameter values in the IH case corresponding to $\chi_{\min} = 7.82429$

Parameter	BF	Parameter	BF	Parameter	BF
τ	$0.344 + 3.36i$	$m_{\eta^\pm}$	7598.89 GeV	M_1	9345.7 GeV
M_2	2463.32 GeV	σ_ν/ρ_ν	$0.0850 - 0.0593i$	α_ν/ρ_ν	-0.3047
β_ν/ρ_ν	$0.1057 - 0.3162i$	δ_l	$-0.4228 - 0.4928i$	α_l	0.0022
β_l	63.991	γ_l	0.465	σ_ℓ	$-0.002617 - 0.01258i$
s_{12}	0.5798	s_{23}	0.6612	s_{13}	0.1514
Δm^2_{sol}	7.476×10^{-5} eV^2	Δm^2_{atm}	2.482×10^{-3} eV^2	δ_{CP}	182.212°
α_{21}	285.241°	$\sum D_\nu$	0.0989 eV	$\langle m_{ee}\rangle$	0.0155 eV

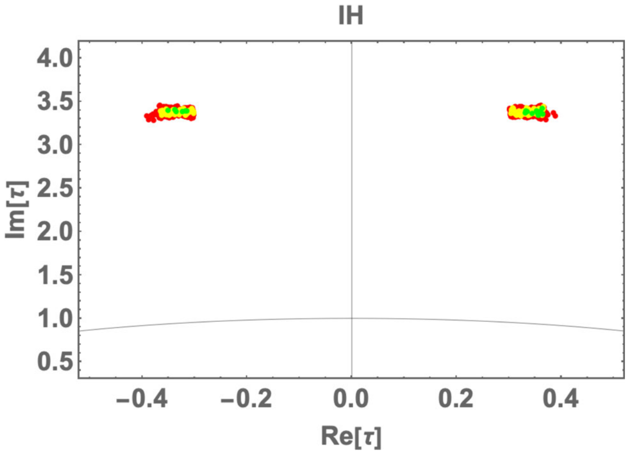

Fig. 8 Scatter plot for Re[τ] *vs.* Im[τ]. The red, yellow, green and blue points correspond to $3\sigma - 5\sigma$, $2\sigma - 3\sigma$, $1\sigma - 2\sigma$, and $0\sigma - 1\sigma$, respectively

with mass $M_i = \zeta_i v_\sigma/\sqrt{2}$ in Eq. (III.8). The PQ symmetry is spontaneously broken at a scale $f_{\text{PQ}} = \langle\sigma\rangle = v_\sigma/\sqrt{2}$, leading to the axion decay constant

$$f_a = \frac{f_{\text{PQ}}}{N} = \frac{v_\sigma}{\sqrt{2}N}\ , \tag{V.1}$$

where N is the color anomaly factor. To be viable, the axion solution to the strong CP problem requires a nonvanishing anomaly factor N to ensure an axion-gluon coupling. As expected, in this model, N depends on the multiplicity of the colored fermions n_Ψ and on the Ψ_L PQ charge ω. Since they are $SU(2)$ singlets, we get

$$\begin{aligned} N &= 2\, n_\Psi\, \omega\, (2n \pm 1)\; T(1,0) \\ &= 2\omega \end{aligned} \tag{V.2}$$

with $T(1,0)$ the Dynkin index of the SU(3)$_c$ representation $\mathbf{3} \sim (1,0)$, which is 1/2. By selecting the minimal multiplicity and setting $\omega = \frac{1}{2}$, we find $N = 1$, consistent with the original KSVZ axion model [9,10].

The axion is coupled to a colored fermion Ψ_i via an axial-vector current,

$$J_a^5 = \frac{\omega}{2N}\left(\frac{\partial_\mu a}{f_a}\right)\sum_{i=1}^{2}\overline{\Psi_i}\gamma^\mu\gamma^5\Psi_i. \tag{V.3}$$

The derivative coupling of the axion is just a current coupling to ABJ anomaly for Ψ_i and we can obtain a Lagragian term with the coupling of a to the dual field strength tensor of the gluons $G_{\mu\nu}$,

$$\mathcal{L} = N\frac{a}{f_a}\frac{g_s^2}{32\pi^2}G_{\mu\nu}\tilde{G}_{\mu\nu}, \tag{V.4}$$

where $\tilde{G}_{\mu\nu} \equiv \epsilon_{\mu\nu\rho\sigma}G^{\rho\sigma}/2$.

The QCD axion mass derived from a non-perturbative potential at next-to-leading order is given by [54]

$$m_a = 5.70(7)\left(\frac{10^{12}\text{GeV}}{f_a}\right)\mu\text{eV}\ . \tag{V.5}$$

This relation between m_a and f_a is a model-independent prediction of the QCD axion if the only explicit breaking of the PQ symmetry is by nonperturbative QCD effects. In Sect. 5.2, we will briefly demonstrate how the DM relic density constrains f_a, leading to an estimation of the axion mass m_a.

Axions have been extensively searched for in numerous experiments, primarily through the axion-photon coupling as described in the effective Lagrangian given by

$$\mathcal{L} = \frac{g_{a\gamma\gamma}}{4}aF_{\mu\nu}\tilde{F}^{\mu\nu}, \tag{V.6}$$

where $F_{\mu\nu}$ represents the photon field strength and $\tilde{F}_{\mu\nu}$ denotes its dual. Consequently, the strength of the axion-photon coupling is crucial for experimental axion searches. In this model, since the only chiral fermions with non-zero PQ charges are Ψ_i and they are $SU(2)_L$ singlets, the ratio of the electromagnetic and color anomaly factors, E/N to be zero, which results in the axion-to-photon coupling $g_{a\gamma\gamma}$ to be

$$g_{a\gamma\gamma} = \frac{\alpha_e}{2\pi f_a}\left[\frac{E}{N} - 1.92(4)\right] = -1.92(4)\frac{\alpha_e}{2\pi f_a}. \tag{V.7}$$

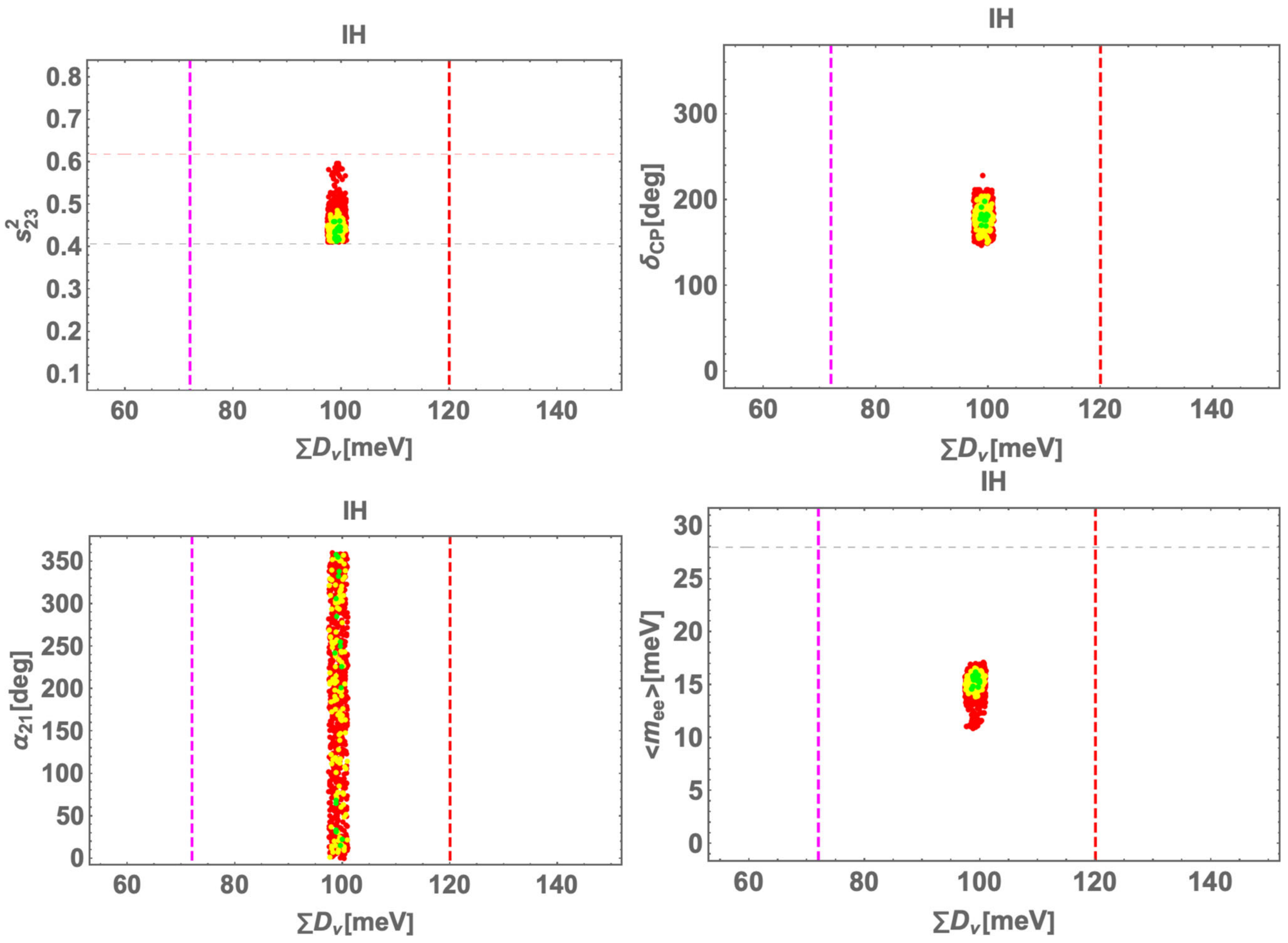

Fig. 9 Plots for **a** s^2_{23}, **b** $\delta_{\rm CP}$, **c** α_{21}, **d** $\langle m_{ee}\rangle$ *vs.* $\sum D_\nu$. The colors of the points carry the same meanings as in Fig. 2

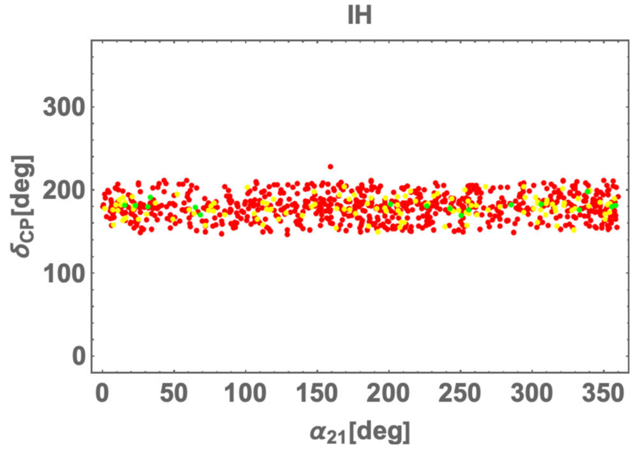

Fig. 10 Plot for the allowed regions of the parameter space (α_{21}, $\delta_{\rm CP}$). The colors of the points carry the same meanings as in Fig. 2

Using the value of f_a constrained by the relic density discussed in Sect. 5.2, we can determine $g_{a\gamma\gamma}(\sim -8\times 10^{-15}$ GeV^{-1}). This result can be interpreted as a lower bound to $g_{a\gamma\gamma}$. Axions can couple to nucleons as $c_N(\partial_\mu a/2f_a)\bar{N}\gamma^\mu\gamma_5 N$. For KSVZ-like models, the axion couplings to proton and neutron are given respectively by $c_p = -0.47(3)$ and $c_n = -0.02(3)$ [54]. By fixing f_a as above, we can also determine the coupling strength $c_N/(2f_a)$. The results of the axion parameter presented in this work are consistent with the current indirect astrophysical and cosmological observations, as well as constraints from laboratory searches (for reviews see Refs. [19,20]).

5.2 Axion dark matter

Axions are a promising dark matter (DM) candidate due to their naturally light mass, weak coupling with ordinary matter, cosmological stability, and potential for nonthermal production in the early Universe. Axion DM can be produced through the misalignment mechanism [16–18], which results in a relic density given by [19]

$$\Omega_{a,mis}h^2 \simeq \Omega_{\rm CDM}h^2\langle\theta_0^2\rangle\left(\frac{f_a}{2\times 10^{11}\ {\rm GeV}}\right)^{\frac{7}{6}}, \qquad ({\rm V.8})$$

where the free parameter $\langle\theta_0^2\rangle$ denotes the initial average misalignment angle squared, which depends on whether PQ symmetry is broken before or after inflation. In the latter case, $\langle\theta_0^2\rangle$ is estimated to be 2.15^2 based on the periodic axion potential including anharmonicities [19,55]. The observed cold DM (CDM) relic abundance obtained by Planck is $\Omega_{\rm CDM}h^2 = 0.1200 \pm 0.0012$ [4]. Then, assuming the axion generated through the misalignment constitutes 100% of CDM, we get $f_a = 2.7 \times 10^{11}$ GeV from Eq. (V.8). Consequently, the axion mass is estimated to be 21.1μeV from Eq. (V.5). If the PQ symmetry is broken after inflation, the formation and decay of cosmic strings and domain walls also contribute significantly to the relic axion abundance. Incorporating these contributions, the total relic density is estimated to be [56],

$$\Omega_{a,tot}h^2 = (1.6 \pm 0.4) \times 10^{-2} \times \left(\frac{f_a}{10^{10}\ \text{GeV}}\right)^{(6+n)/(4+n)} \tag{V.9}$$

where QCD scale is taken to be 400 MeV and $n = 6.68$. The result implies $\Omega_{a,tot}h^2 \simeq 3\Omega_{a,mis}h^2$. This additional contributions effectively reduce the value of the axion decay constant f_a required to match the observed dark matter density, leading to a correspondingly higher axion mass. Assuming that $\Omega_{a,tot}h^2$ accounts for 100% of CDM, the value of f_a is shifted to $(4.6 - 7.2) \times 10^{10}$ GeV, with the corresponding axion mass in the range $(0.8 - 1.3) \times 10^{-4}$ eV. For these values of f_a, the axion-to-photon coupling $g_{a\gamma\gamma}$ is predicted to be approximately $-(3 \sim 5) \times 10^{-14}\ \text{GeV}^{-1}$ as given by Eq. (V.7). These parameter values fall within the permissible region of the hadronic parameter space, as discussed in [19].

In the pre-inflationary scenario, we assume that the masses of exotic fermions and scalars exceed the reheating temperature of the Universe, i.e. $(M_{1,2}, m_{\chi_1},\ m_{S_{1,2,3}}) \gtrsim T_{\rm RH} \gtrsim 4.7$ MeV, where the lower limit on $T_{\rm RH}$ is set by Big Bang nucleosynthesis [57]. As a result, the abundance of stable baryonic or charged relics, as well as topological defects, would be erased during inflation. In this scenario, the axion imprints itself on primordial fluctuations, reflected in the cosmic microwave background anisotropies and large-scale structure. The isocurvature fluctuations generated are constrained by cosmic microwave background data [58], resulting in an upper bound on the inflationary scale H_I [59]:

$$H_I \lesssim \frac{0.9 \times 10^7}{\Omega_a h^2/\Omega_{\rm CDM}h^2}\left(\frac{\langle\theta_0\rangle}{\pi}\frac{f_a}{10^{11}\ \text{GeV}}\right) \text{GeV} \lesssim 2.0 \times 10^7\ \text{GeV}, \tag{V.10}$$

where the numerical value for the upper bound is derived, assuming axions constitute all DM, from the threshold value of $\langle\theta_0\rangle$ as adopted from the results in [60].

Axion DM can also be produced through kinetic misalignment mechanism [61]. In the kinetic misalignment mechanism, the axion field has a significant initial velocity $\dot{a}_0$ or kinetic energy. Thus, the axion starts its evolution with both a misalignment angle θ_0 and a non-zero velocity $\dot{a}_0$. Once the axion field starts oscillating, it behaves like CDM with a relic density that can be estimated. In the kinetic misalignment scenario, the relic density can be modified due to the initial kinetic energy. If the kinetic energy density at a temperature is larger than the potential barrier, kinetic misalignment occurs and the axion oscillations are delayed until the kinetic energy is below that of the potential [61]. By considering the effects of inflation on kinetic misalignment and parametric resonance, the authors in [62] obtained $4 \times 10^8 < f_a/[\text{GeV}] < 10^{11}$ for consistent production of axion DM. For the result of f_a, the axion mass is estimated to be 57 μeV $\lesssim m_a \lesssim$ 14.25 meV from Eq. (V.5), and the axion-to-photon coupling is predicted to be $-2.2 \times 10^{-14} \lesssim g_{a\gamma\gamma} \times [\text{GeV}] \lesssim -5.6 \times 10^{-12}$ from Eq. (V.7).

Future helioscope and haloscope experiments, including IAXO, ADMX, MADMAX, and CAPP, are expected to probe unexplored regions of the parameter space for the axion-photon coupling $|g_{a\gamma\gamma}|$ and the axion mass m_a significantly advancing our ability to detect or constrain axion DM models. As is known, the region of $|g_{a\gamma\gamma}|$ around $10^{-12} \sim 10^{-11}\ \text{GeV}^{-1}$ will be probed at IAXO [63]. The full ladscape of QCD axion models for masses 1 μeV $\lesssim m_a \lesssim$ 100 μeV and 50 μeV $\lesssim m_a \lesssim$ 120 μeV will be probed at ADMX [64] and MADMAX [65], respectively. In addition, CAPP aims to achieve a sensitivity to $|g_{a\gamma\gamma}|$ as low as $10^{-16}\ \text{GeV}^{-1}$, with a focus on the axion mass ranging from approximately 1μeV to 10μeV, and extending their search to higher mass ranges up to 30μeV [66]. Therefore, the predicted values of $g_{a\gamma\gamma}$ and m_a in our model may fall within the reach of upcoming experimental searches.

Axions can also be probed indirectly via astrophysical and cosmological observations, particularly through the decay or conversion of axion dark matter into photons under strong magnetic fields or in dense environments [19,67]. These indirect searches cover a wide mass range, from ultralight axions ($m_a \lesssim 10^{-14}$ eV) to masses above the MeV scale. In the context of our model, we focus on the region $m_a \sim \mathcal{O}(10\text{–}100)$ μeV, which is predicted with axion dark matter. Axion to photon conversion in the magnetospheres of neutron stars, particularly near the Galactic Center, has been probed by the Breakthrough Listen project using radio surveys in the C-band. These studies constrain the coupling to $g_{a\gamma\gamma} \lesssim 10^{-11}\ \text{GeV}^{-1}$ for axion masses between 15 μeV and 35 μeV [68]. Similarly, radio data from the Bullet Cluster (1E 0657-55.8) yield an upper bound on the axion-photon coupling of $g_{a\gamma\gamma} \sim 10^{-12}\text{–}10^{-11}\ \text{GeV}^{-1}$ for $m_a \sim 10\text{–}30$ μeV [69]. Axions may also influence stellar evolution by enhancing cooling processes such as the Primakoff effect. Observations of horizontal branch stars in globular clusters place a strong upper limit of $g_{a\gamma\gamma} \lesssim 6.6 \times 10^{-11}\ \text{GeV}^{-1}$ [70]. This is consistent with bounds from the CAST helioscope, which similarly constrains $g_{a\gamma\gamma}$ for $m_a \lesssim 0.02$ eV [71]. In addition, recent constraints derived from SN 1987A gamma ray data have improved limits on axion-photon couplings by accounting for axion to photon conversion in the magnetic field of the supernova progenitor itself. These analyses yield limits of $g_{a\gamma\gamma} \lesssim \text{few} \times 10^{-11}\ \text{GeV}^{-1}$ for $10^{-6} \lesssim m_a \lesssim 10^{-3}$ eV, representing an order-of-magnitude improvement over earlier bounds based solely on conversion in the Galactic magnetic field [72]. In our model, the predicted coupling lies well below those bounds.

6 Conclusions

In this paper, we have constructed a predictive axion model with modular S_3 symmetry to address a connection among seemingly unrelated issues: tiny neutrino masses and mixing, dark matter and the strong CP problem. This was achieved within a novel class of KSVZ axion schemes, containing exotic colored fermions and scalars which act as neutrino-mass mediators at the two-loop level. The radiative generation of neutrino masses at the two-loop level accounts for their smallness, while the neutrino mixing arises from the modular S_3 symmetry that we consider. We have demonstrated that the combination of PQ symmetry and Z_2 symmetry, integrated with modular S_3 and the appropriate assignment of modular weights to the fields, can effectively constrain the forms of Yukawa interactions and the scalar potential. This framework is applicable to both SUSY (holomorphic) and non-SUSY (non-holomorphic) scenarios, and ensures the robustness of the resulting predictions. We have presented the numerical results illustrating how the predictions and physical implications for neutrino masses and mixing differ between the holomorphic and non-holomorphic cases. In the holomorphic case, only NH is favored by the neutrino oscillation data , whereas in the non-holomorphic case, both NH and IH are consistent with experimental data. Under reasonable conditions, we have ignored the subleading corrections such as those from higher-dimensional operators, RG running, and SUSY-breaking effects, and focused on the leading-order predictions. This scenario also predicts lepton flavor violations with a small rate and neutrinoless double beta decay, with the amplitude proportional to the effective neutrino mass being well below the current experimental bounds. Since the lightest neutrino mass vanishes, the sum of neutrino masses is written in terms of two experimental values Δm^2_{atm} and Δm^2_{sol}. That leads $\sum D_\nu \simeq 50(100)$ meV in the NH(IH) case which is in good agreement with the recent combined DESI and CMB data (cosmological observations).

Furthermore, we have demonstrated that the axion emerging from our framework not only resolves the strong CP problem but also serves as a viable dark matter candidate across multiple cosmological scenarios, including post-inflationary string-induced contributions and kinetic misalignment production. The resulting axion decay constant and mass, constrained by the relic density, predict an axion-photon coupling in the range $|g_{a\gamma\gamma}| \sim 10^{-15}$–$10^{-12}\ \text{GeV}^{-1}$, which lies within the reach of upcoming experimental searches such as IAXO, ADMX, MADMAX, and CAPP. Moreover, these predictions remain consistent with existing astrophysical and cosmological bounds. Thus, our model offers a highly testable and unified explanation of neutrino masses, dark matter, and the strong CP problem–linking axion phenomenology and lepton flavor structure through a common modular origin.

Acknowledgements SKK was supported by the National Research Foundation of Korea (NRF) grant funded by the Korea government (MSIT) (No.2023R1A2C1006091). HO is supported by Zhongyuan Talent (Talent Recruitment Series) Foreign Experts Project.

Data Availability Statement This manuscript has no associated data. [Author’s’ comment: Data sharing not applicable to this article as no datasets were generated or analysed during the current study.]

Code Availability Statement This manuscript has no associated code/software. [Author’s comment: Code/Software sharing not applicable to this article as no code/software was generated or analysed during the current study.]

Appendix A: Two-loop integral

Let us briefly show how the two-loop integrals in Eqs. (III.12 and III.13) are derived. The relevant two-loop integral takes the form

$$\int \frac{d^4k_2}{(2\pi)^4} \int \frac{d^4k_1}{(2\pi)^4} \frac{\not{k}_1\not{k}_2}{[k_1^2 - M_\ell^2][k_2^2 - M_m^2][k_1^2 - m_{S_i}^2][k_2^2 - m_{S_j}^2][(k_1+k_2)^2 - m_{\chi_1}^2]}. \tag{A.1}$$

We begin by calulating the k_1 integral:

$$\int \frac{d^4k_1}{(2\pi)^4} \frac{\not{k}_1}{[k_1^2 - M_\ell^2]][k_1^2 - m_{S_i}^2][(k_1+k_2)^2 - m_{\chi_1}^2]} = \frac{i}{(4\pi)^2} \int \frac{[dx]_3}{y-1} \frac{\not{k}_2}{k_2^2 + D_1^2}, \tag{A.2}$$

$$(D_\ell^{i1})^2 = \frac{1}{y(y-1)}(x m_{S_i}^2 + y M_\ell^2 + z m_{\chi_1}^2), \tag{A.3}$$

where $[dx]_3 \equiv dxdydz\delta(1-x-y-z)$. Substituting Eq. (A.2) into the remaining k_2 integral, we obtain

$$\int \frac{d^4k_2}{(2\pi)^4} \frac{k_2^2}{[k_2^2 + (D_\ell^{i1})^2][k_2^2 - M_m^2][k_2^2 - m_{S_j}^2]} = -\frac{i}{(4\pi)^2}\left[\frac{(\zeta_{\ell m}^{i1})^2 \ln[\zeta_{\ell m}^{i1}]}{(-1+\zeta_{\ell m}^{i1})(\zeta_{\ell m}^{i1} - \xi_m^j)} - \frac{(\xi_m^j)^2 \ln[\xi_m^j]}{(-1+\xi_m^j)(\zeta_{\ell m}^{i1} - \xi_m^j)}\right], \tag{A.4}$$

$$\zeta_{\ell m}^{i1} \equiv -\frac{(D_\ell^{i1})^2}{M_m^2}, \quad \xi_m^j \equiv \frac{m_{S_j}^2}{M_m^2}. \tag{A.5}$$

Notice here that the logarithmic divergence vanishes when we sum over the indices i, j due to the unitarity of the mixing matrix of U in Eq. (II.5). Using Eqs. (A.2)–(A.5), we can obtain the expressions given in Eqs. (III.12 and III.13).

Appendix B: S_3 symmetry

Due to its three dimensional representation can be decomposed as $\mathbf{3}_S = \mathbf{2} \oplus \mathbf{1}_S$ or $\mathbf{3}_A = \mathbf{2} \oplus \mathbf{1}_A$. The multiplication rules among doublets and singlets are given by [42] as follows;

$$\begin{pmatrix} a_1 \\ a_2 \end{pmatrix}_{\mathbf{2}} \otimes \begin{pmatrix} b_1 \\ b_2 \end{pmatrix}_{\mathbf{2}} = (a_1b_1 + a_2b_2)_{\mathbf{1}_S} \oplus (a_1b_2 - a_2b_1)_{\mathbf{1}_A} \oplus \begin{pmatrix} a_1b_2 + a_2b_1 \\ a_1b_1 - a_2b_2 \end{pmatrix}_{\mathbf{2}}, \tag{B.1}$$

$$\begin{pmatrix} a_1 \\ a_2 \end{pmatrix}_{\mathbf{2}} \otimes (y')_{\mathbf{1}_S} = \begin{pmatrix} a_1y' \\ a_2y' \end{pmatrix}_{\mathbf{2}}, \quad \begin{pmatrix} a_1 \\ a_2 \end{pmatrix}_{\mathbf{2}} \otimes (y')_{\mathbf{1}_A} = \begin{pmatrix} -a_2y' \\ a_1y' \end{pmatrix}_{\mathbf{2}}, \tag{B.2}$$

$$(x)_{\mathbf{1}_S} \otimes (y)_{\mathbf{1}_A} = (xy)_{\mathbf{1}_A}, \quad (x)_{\mathbf{1}_A} \otimes (y)_{\mathbf{1}_A} = (xy)_{\mathbf{1}_S}. \tag{B.3}$$

Appendix C: Modular S_3 symmetry

The modular group $\bar{\Gamma}$ is the group of linear fractional transformation γ acting on the modulus τ, belonging to the upper-half complex plane as:

$$\tau \longrightarrow \gamma\tau = \frac{a\tau + b}{c\tau + d} \quad \text{where} \quad a, b, c, d \in \mathbb{Z} \quad \text{and} \quad ad - bc = 1, \quad \text{Im}[\tau] > 0, \tag{C.1}$$

which is isomorphic to $PSL(2,\mathbb{Z}) = SL(2,\mathbb{Z})/\{I, -I\}$ transformation. This modular transformation is generated by S and T,

$$S : \tau \longrightarrow -\frac{1}{\tau} \quad T : \tau \longrightarrow \tau + 1 \tag{C.2}$$

which satisfy the following algebraic relations,

$$S^2 = T^2 = (ST)^3 = \mathbb{1}. \tag{C.3}$$

We introduce the series of groups $\Gamma(N)$ $(N = 1, 2, 3, \dots)$ defined by

$$\Gamma(N) = \left\{ \begin{pmatrix} a & b \\ c & d \end{pmatrix} \in SL(2,\mathbb{Z}), \quad \begin{pmatrix} a & b \\ c & d \end{pmatrix} = \begin{pmatrix} 1 & 0 \\ 0 & 1 \end{pmatrix} \quad (\text{mod} N) \right\}. \tag{C.4}$$

For $N = 2$, we define $\bar{\Gamma}(2) \equiv \Gamma(2)/\{I, -I\}$. Since the element $-I$ does not belong to $\Gamma(N)$ for $N > 2$, we have $\bar{\Gamma}(N) = \Gamma(N)$, which are infinite normal subgroup of $\bar{\Gamma}$, called principal congruence subgroups. The quotient groups defined as $\Gamma_N \equiv \bar{\Gamma}/\bar{\Gamma}(N)$ are finite modular groups. In this finite groups Γ_N, $T^N = \mathbb{1}$ is imposed. The groups Γ_N with $N = 2, 3, 4, 5$ are isomorphic to S_3, A_4, S_4 and A_5, respectively [27].

Modular forms of level N are holomorphic functions $f(\tau)$ transforming under the action of $\Gamma(N)$ as:

$$f(\gamma\tau) = (c\tau + d)^k f(\tau), \quad \gamma \in \Gamma(N), \tag{C.5}$$

where k is the so-called as the modular weight.

We discuss the modular symmetric theory without supersymmetry. In this paper, we fix the modular S_3 $(N = 2)$ group. Under the modular transformation of Eq. (C.1), fields $\phi^{(I)}$ transform as

$$\phi^{(I)} \rightarrow (c\tau + d)^{-k_I} \rho^{(I)}(\gamma)\phi^{(I)}, \tag{C.6}$$

where $-k_I$ is the modular weight and $\rho^{(I)}(\gamma)$ denotes a unitary representation matrix of $\gamma \in \Gamma(2)$.

The kinetic terms of their scalar fields are derived from the Kähler potential invariant under the modular symmetry up to Kähler transformation given as,

$$K = -h\log(-i\tau + i\bar{\tau}) + \sum_I (-i\tau + i\bar{\tau})^{-k_I} |\phi^{(I)}|^2, \tag{C.7}$$

where h is a positive constant and the scalar $\phi^{(I)}$ has modular weight k_I. Then, the Kähler metric gives the kinetic terms of ϕ as

$$\mathcal{L}_{\text{kin}} = K_{\phi\bar{\phi}} \partial_\mu \bar{\phi}^{(I)} \partial^\mu \phi^{(I)}. \tag{C.8}$$

The final form of the kinetic terms of scalar field is given by

$$\sum_I \frac{|\partial_\mu \phi^{(I)}|^2}{(-i\tau + i\bar{\tau})^{k_I}}, \tag{C.9}$$

which is invariant under the modular transformation. Also, the Lagrangian such as $|\phi^I|^2$ should be invariant under the modular symmetry.

References

1. T. Kajita, Rev. Mod. Phys. **88**(3), 030501 (2016). https://doi.org/10.1103/RevModPhys.88.030501
2. A.B. McDonald, Rev. Mod. Phys. **88**(3), 030502 (2016). https://doi.org/10.1103/RevModPhys.88.030502
3. G. Bertone, D. Hooper, J. Silk, Phys. Rep. **405**, 279–390 (2005). https://doi.org/10.1016/j.physrep.2004.08.031. arXiv:hep-ph/0404175
4. N. Aghanim et al. [Planck], Astron. Astrophys. **641**, A6 (2020) [Erratum: Astron. Astrophys. **652**, C4 (2021)] https://doi.org/10.1051/0004-6361/201833910. arXiv:1807.06209 [astro-ph.CO]
5. R.D. Peccei, H.R. Quinn, Phys. Rev. Lett. **38**, 1440–1443 (1977). https://doi.org/10.1103/PhysRevLett.38.1440
6. R.D. Peccei, H.R. Quinn, Phys. Rev. D **16**, 1791–1797 (1977). https://doi.org/10.1103/PhysRevD.16.1791
7. S. Weinberg, Phys. Rev. Lett. **40**, 223–226 (1978). https://doi.org/10.1103/PhysRevLett.40.223
8. F. Wilczek, Phys. Rev. Lett. **40**, 279–282 (1978). https://doi.org/10.1103/PhysRevLett.40.279
9. J.E. Kim, Phys. Rev. Lett. **43**, 103 (1979). https://doi.org/10.1103/PhysRevLett.43.103
10. M.A. Shifman, A.I. Vainshtein, V.I. Zakharov, Nucl. Phys. B **166**, 493–506 (1980). https://doi.org/10.1016/0550-3213(80)90209-6
11. A.R. Zhitnitsky, Sov. J. Nucl. Phys. **31**, 260 (1980)
12. M. Dine, W. Fischler, M. Srednicki, Phys. Lett. B **104**, 199–202 (1981). https://doi.org/10.1016/0370-2693(81)90590-6
13. Z. Tao, Phys. Rev. D **54**, 5693–5697 (1996). https://doi.org/10.1103/PhysRevD.54.5693. arXiv:hep-ph/9603309
14. E. Ma, Phys. Rev. D **73**, 077301 (2006). https://doi.org/10.1103/PhysRevD.73.077301. arXiv:hep-ph/0601225
15. M. Hirsch, R.A. Lineros, S. Morisi, J. Palacio, N. Rojas, J.W.F. Valle, JHEP **10**, 149 (2013). https://doi.org/10.1007/JHEP10(2013)149. arXiv:1307.8134 [hep-ph]
16. J. Preskill, M.B. Wise, F. Wilczek, Phys. Lett. B **120**, 127–132 (1983). https://doi.org/10.1016/0370-2693(83)90637-8
17. L.F. Abbott, P. Sikivie, Phys. Lett. B **120**, 133–136 (1983). https://doi.org/10.1016/0370-2693(83)90638-X
18. M. Dine, W. Fischler, Phys. Lett. B **120**, 137–141 (1983). https://doi.org/10.1016/0370-2693(83)90639-1
19. L. Di Luzio, M. Giannotti, E. Nardi, L. Visinelli, Phys. Rept. **870**, 1–117 (2020). https://doi.org/10.1016/j.physrep.2020.06.002. arXiv:2003.01100 [hep-ph]
20. C.B. Adams, N. Aggarwal, A. Agrawal, R. Balafendiev, C. Bartram, M. Baryakhtar, H. Bekker, P. Belov, K.K. Berggren, A. Berlin et al., arXiv:2203.14923 [hep-ex]
21. G. Arcadi, M. Dutra, P. Ghosh, M. Lindner, Y. Mambrini, M. Pierre, S. Profumo, F.S. Queiroz, Eur. Phys. J. C **78**(3), 203 (2018). https://doi.org/10.1140/epjc/s10052-018-5662-y. arXiv:1703.07364 [hep-ph]
22. R.N. Mohapatra, G. Senjanovic, Z. Phys. C **17**, 53–56 (1983). https://doi.org/10.1007/BF01577819
23. P. Langacker, R.D. Peccei, T. Yanagida, Mod. Phys. Lett. A **1**, 541 (1986). https://doi.org/10.1142/S0217732386000683
24. M. Shin, Phys. Rev. Lett. **59**, 2515 (1987) [erratum: Phys. Rev. Lett. **60**, 383 (1988)] https://doi.org/10.1103/PhysRevLett.59.2515
25. X.G. He, R.R. Volkas, Phys. Lett. B **208**, 261 (1988) [Erratum: Phys. Lett. B **218**, 508 (1989)] https://doi.org/10.1016/0370-2693(88)90427-3
26. A. Batra, H.B. Câmara, F.R. Joaquim, R. Srivastava, J.W.F. Valle, Phys. Rev. Lett. **132**(5), 051801 (2024). https://doi.org/10.1103/PhysRevLett.132.051801. arXiv:2309.06473 [hep-ph]
27. R. de Adelhart Toorop, F. Feruglio, C. Hagedorn, Nucl. Phys. B **858**, 437–467 (2012). https://doi.org/10.1016/j.nuclphysb.2012.01.017. arXiv:1112.1340 [hep-ph]
28. F. Feruglio, https://doi.org/10.1142/9789813238053_0012. arXiv:1706.08749 [hep-ph]
29. G.J. Ding, S.F. King, Rep. Prog. Phys. **87**(8), 084201 (2024). https://doi.org/10.1088/1361-6633/ad52a3. arXiv:2311.09282 [hep-ph]
30. T. Kobayashi, K. Tanaka, T.H. Tatsuishi, Phys. Rev. D **98**(1), 016004 (2018). https://doi.org/10.1103/PhysRevD.98.016004. arXiv:1803.10391 [hep-ph]
31. T. Kobayashi, Y. Shimizu, K. Takagi, M. Tanimoto, T.H. Tatsuishi, H. Uchida, Phys. Lett. B **794**, 114–121 (2019). https://doi.org/10.1016/j.physletb.2019.05.034. arXiv:1812.11072 [hep-ph]
32. T. Kobayashi, Y. Shimizu, K. Takagi, M. Tanimoto, T.H. Tatsuishi, PTEP **2020**(5), 053B05 (2020). https://doi.org/10.1093/ptep/ptaa055. arXiv:1906.10341 [hep-ph]
33. G. Altarelli, F. Feruglio, Rev. Mod. Phys. **82**, 2701–2729 (2010). https://doi.org/10.1103/RevModPhys.82.2701. arXiv:1002.0211 [hep-ph]
34. H. Ishimori, T. Kobayashi, H. Ohki, Y. Shimizu, H. Okada, M. Tanimoto, Prog. Theor. Phys. Suppl. **183**, 1–163 (2010). https://doi.org/10.1143/PTPS.183.1. arXiv:1003.3552 [hep-th]
35. H. Ishimori, T. Kobayashi, H. Ohki, H. Okada, Y. Shimizu, M. Tanimoto, Lect. Notes Phys. **858**, 1–227 (2012). https://doi.org/10.1007/978-3-642-30805-5
36. D. Hernandez, A.Y. Smirnov, Phys. Rev. D **86**, 053014 (2012). https://doi.org/10.1103/PhysRevD.86.053014. arXiv:1204.0445 [hep-ph]
37. S.F. King, C. Luhn, Rep. Prog. Phys. **76**, 056201 (2013). https://doi.org/10.1088/0034-4885/76/5/056201. arXiv:1301.1340 [hep-ph]
38. G.J. Ding, F. Feruglio, X.G. Liu, JHEP **01**, 037 (2021). https://doi.org/10.1007/JHEP01(2021)037. arXiv:2010.07952 [hep-th]
39. G.J. Ding, J.N. Lu, S.T. Petcov, B.Y. Qu, JHEP **01**, 191 (2025). https://doi.org/10.1007/JHEP01(2025)191. arXiv:2408.15988 [hep-ph]
40. B.Y. Qu, G.J. Ding, JHEP **08**, 136 (2024). https://doi.org/10.1007/JHEP08(2024)136. arXiv:2406.02527 [hep-ph]
41. J.C. Criado, F. Feruglio, SciPost Phys. **5**(5), 042 (2018). https://doi.org/10.21468/SciPostPhys.5.5.042. arXiv:1807.01125 [hep-ph]
42. P.P. Novichkov, J.T. Penedo, S.T. Petcov, A.V. Titov, JHEP **07**, 165 (2019). https://doi.org/10.1007/JHEP07(2019)165. arXiv:1905.11970 [hep-ph]
43. M. Aoki, T. Toma, JCAP **09**, 016 (2014). https://doi.org/10.1088/1475-7516/2014/09/016. arXiv:1405.5870 [hep-ph]
44. S. Vagnozzi, E. Giusarma, O. Mena, K. Freese, M. Gerbino, S. Ho, M. Lattanzi, Phys. Rev. D **96**(12), 123503 (2017). https://doi.org/10.1103/PhysRevD.96.123503. arXiv:1701.08172 [astro-ph.CO]
45. A.G. Adame et al. [DESI], arXiv:2404.03002 [astro-ph.CO]
46. A. Gando et al. [KamLAND-Zen Collaboration], Phys. Rev. Lett. **117**(8), 082503 (2016) [Addendum: Phys. Rev. Lett. **117**, no. 10, 109903 (2016)] https://doi.org/10.1103/PhysRevLett.117.109903. arXiv:1605.02889 [hep-ex]
47. A. Gando et al., Phys. Rev. Lett. **130**(5), 051801 (2023). https://doi.org/10.1103/PhysRevLett.130.051801. arXiv:2203.02139 [hep-ex]
48. I. Esteban, M.C. Gonzalez-Garcia, M. Maltoni, T. Schwetz, A. Zhou, JHEP **09**, 178 (2020). https://doi.org/10.1007/JHEP09(2020)178. arXiv:2007.14792 [hep-ph]
49. S. Baek, T. Nomura, H. Okada, Phys. Lett. B **759**, 91 (2016). https://doi.org/10.1016/j.physletb.2016.05.055. arXiv:1604.03738 [hep-ph]

50. M. Lindner, M. Platscher, F.S. Queiroz, Phys. Rep. **731**, 1 (2018). https://doi.org/10.1016/j.physrep.2017.12.001. arXiv:1610.06587 [hep-ph]
51. A.M. Baldini et al., [MEG Collaboration], Eur. Phys. J. C **76**(8), 434 (2016). arXiv:1605.05081 [hep-ex]
52. F. Renga [MEG Collaboration], Hyperfine Interact. **239**(1), 58 (2018). arXiv:1811.05921 [hep-ex]
53. B. Aubert et al. [BaBar Collaboration], Phys. Rev. Lett. **104**, 021802 (2010). arXiv:0908.2381 [hep-ex]
54. G. Grilli di Cortona, E. Hardy, J. Pardo Vega, G. Villadoro, JHEP **01**, 034 (2016). https://doi.org/10.1007/JHEP01(2016)034. arXiv:1511.02867 [hep-ph]
55. L. Visinelli, P. Gondolo, Phys. Rev. D **80**, 035024 (2009). https://doi.org/10.1103/PhysRevD.80.035024. arXiv:0903.4377 [astro-ph.CO]
56. M. Kawasaki, K. Saikawa, T. Sekiguchi, Phys. Rev. D **91**(6), 065014 (2015). https://doi.org/10.1103/PhysRevD.91.065014. arXiv:1412.0789 [hep-ph]
57. P.F. de Salas, M. Lattanzi, G. Mangano, G. Miele, S. Pastor, O. Pisanti, Phys. Rev. D **92**(12), 123534 (2015). https://doi.org/10.1103/PhysRevD.92.123534. arXiv:1511.00672 [astro-ph.CO]
58. M. Beltran, J. Garcia-Bellido, J. Lesgourgues, Phys. Rev. D **75**, 103507 (2007). https://doi.org/10.1103/PhysRevD.75.103507. arXiv:hep-ph/0606107
59. L. Di Luzio, F. Mescia, E. Nardi, Phys. Rev. Lett. **118**(3), 031801 (2017). https://doi.org/10.1103/PhysRevLett.118.031801. arXiv:1610.07593 [hep-ph]
60. S. Borsanyi, Z. Fodor, J. Guenther, K.H. Kampert, S.D. Katz, T. Kawanai, T.G. Kovacs, S.W. Mages, A. Pasztor, F. Pittler et al., Nature **539**(7627), 69–71 (2016). https://doi.org/10.1038/nature20115. arXiv:1606.07494 [hep-lat]
61. R.T. Co, L.J. Hall, K. Harigaya, Phys. Rev. Lett. **124**(25), 251802 (2020). https://doi.org/10.1103/PhysRevLett.124.251802. arXiv:1910.14152 [hep-ph]
62. R.T. Co, L.J. Hall, K. Harigaya, K.A. Olive, S. Verner, JCAP **08**, 036 (2020). https://doi.org/10.1088/1475-7516/2020/08/036. arXiv:2004.00629 [hep-ph]
63. E. Armengaud, F.T. Avignone, M. Betz, P. Brax, P. Brun, G. Cantatore, J.M. Carmona, G.P. Carosi, F. Caspers, S. Caspi et al., JINST **9**, T05002 (2014). https://doi.org/10.1088/1748-0221/9/05/T05002. arXiv:1401.3233 [physics.ins-det]
64. I. Stern, PoS **ICHEP2016**, 198 (2016). https://doi.org/10.22323/1.282.0198. arXiv:1612.08296 [physics.ins-det]
65. S. Beurthey, N. Böhmer, P. Brun, A. Caldwell, L. Chevalier, C. Diaconu, G. Dvali, P. Freire, E. Garutti, C. Gooch et al., arXiv:2003.10894 [physics.ins-det]
66. Y.K. Semertzidis, J.E. Kim, S. Youn, J. Choi, W. Chung, S. Haciomeroglu, D. Kim, J. Kim, B. Ko, O. Kwon et al., arXiv:1910.11591 [physics.ins-det]
67. C.A.J. O'Hare, PoS **COSMICWISPers**, 040 (2024). https://doi.org/10.22323/1.454.0040. arXiv:2403.17697 [hep-ph]
68. J.W. Foster, S.J. Witte, M. Lawson, T. Linden, V. Gajjar, C. Weniger, B.R. Safdi, Phys. Rev. Lett. **129**(25), 251102 (2022). https://doi.org/10.1103/PhysRevLett.129.251102. arXiv:2202.08274 [astro-ph.CO]
69. M.H. Chan, Sci. Rep. **11**(1), 20087 (2021). https://doi.org/10.1038/s41598-021-99495-3. arXiv:2109.11734 [astro-ph.CO]
70. A. Ayala, I. Domínguez, M. Giannotti, A. Mirizzi, O. Straniero, Phys. Rev. Lett. **113**(19), 191302 (2014). https://doi.org/10.1103/PhysRevLett.113.191302. arXiv:1406.6053 [astro-ph.SR]
71. V. Anastassopoulos et al. [CAST], Nat. Phys. **13**, 584–590 (2017). https://doi.org/10.1038/nphys4109. arXiv:1705.02290 [hep-ex]
72. C.A. Manzari, Y. Park, B.R. Safdi, I. Savoray, Phys. Rev. Lett. **133**(21), 211002 (2024). https://doi.org/10.1103/PhysRevLett.133.211002. arXiv:2405.19393 [hep-ph]